

Charge-loop current order and Z_3 nematicity mediated by bond order fluctuations in kagome metals

Rina Tazai¹, Youichi Yamakawa², and Hiroshi Kontani²

¹*Yukawa Institute for Theoretical Physics, Kyoto University, Kyoto 606-8502, Japan*

²*Department of Physics, Nagoya University, Furo-cho, Nagoya 464-8602, Japan.*

(Dated: May 19, 2025)

Recent experiments on geometrically frustrated kagome metal AV_3Sb_5 ($A=K, Rb, Cs$) have revealed the emergence of the charge loop current (cLC) order near the bond order (BO) phase. However, the origin of the cLC and its interplay with other phases have been uncovered. Here, we propose a novel mechanism of the cLC state, by focusing on the BO phase common in kagome metals. The BO fluctuations in kagome metals, which emerges due to the Coulomb interaction and the electron-phonon coupling, mediate the odd-parity particle-hole condensation that gives rise to the topological current order. Furthermore, the predicted cLC+BO phase gives rise to the Z_3 -nematic state in addition to the giant anomalous Hall effect. The present theory predicts the close relationship between the cLC, the BO, and the nematicity, which is significant to understand the cascade of quantum electron states in kagome metals.

Introduction

Recent discovery of the kagome-lattice metal AV_3Sb_5 ($A=K, Rb, Cs$) shown in Fig. 1 **a** has opened the way to study the unique physics of geometrically frustrated metals with strong correlation [1–3]. In CsV_3Sb_5 , the formation of the 2×2 Star-of-David or Tri-Hexagonal density wave (DW) was detected by scanning tunneling microscopy (STM) at $T \approx 90$ K at ambient pressure [4, 5]. It is presumably the triple- q ($3Q$) bond order (BO) shown in Fig. 1 **b**, which is the even-parity modulation in the hopping integral δt_{ij}^b (=real) [6–12]. Below the BO transition temperature T_{BO} , superconductivity (SC) with highly anisotropic gap emerges for $A=Cs$ [13, 14], and the gap structure changes to isotropic by introducing impurities. Also, nodal to nodeless crossover is induced by the external pressure in $A=Rb, K$ [15]. These results are naturally understood based on the BO fluctuation mechanism [12].

More recently, the non-trivial time reversal symmetry breaking (TRSB) order at T_{TRSB} attracts considerable attention. It has been reported by μ SR study [15–18], Kerr rotation analysis [19], field-tuned chiral transport study [20] and STM measurements [4, 20]. The transition temperature T_{TRSB} is close to T_{BO} in many experiments, while the TRSB order parameter is strongly magnified at $T^* \approx 35$ K for $A=Cs$ [16, 18, 20] and $T^* \approx 50$ K for $A=Rb$ [15]. Recently, magnetic torque measurement reveals the TRSB order associated with the rotational symmetry breaking, which is called the nematic order, at $T^* \approx 130$ K [21]. In contrast, TRSB was not reported by different experimental groups using the Kerr rotation [22] and STM [23] measurements. Thus, the TRSB onset temperature is still under debate. The chiral cLC is driven by the additional odd-parity hopping integral δt_{ij}^c (=imaginary), and the accompanied topological charge-current [24] gives the giant anomalous Hall effect (AHE) below $T \approx 35$ K [25, 26]. The correlation-driven topo-

logical phase in kagome metals is very unique, while its mechanism is still unknown.

In addition to the cascade of quantum phase transitions, the emergent nematic order inside the BO and the cLC phases attracts great attention. The nematic transition is clearly observed by the elastoresistance [27], the scanning birefringence [19], and the STM [5] studies. In addition, nematic SC states have been reported [23, 28]. Thus, kagome metals provide a promising platform for exploring the interplay between electron correlations and topological nature.

To understand the rich quantum phases in kagome metals, lots of theoretical studies have been performed [6–12, 29–31]. Each BO and cLC order is explained by introducing various off-site interactions in the mean-field approximation (MFA) [9, 29, 32, 33], while a fine-tuning of off-site interactions is necessary to explain the cascade of phase transitions. On the other hand, beyond-MFA mechanisms have been developed to explain the rich phase transitions [34–45]. For example, strong interplay between the magnetism, nematicity and SC in Fe-based superconductors and other strongly correlated metals were understood by beyond-MFA mechanisms [36–45]. It is urgent and important to elucidate why the BO and cLC orders/fluctuations coexist in the study of kagome metals. For example, these fluctuations will mediate non-BCS SC [12] and exotic pair-density-wave states [46–48].

In this paper, we reveal that the cLC order is mediated by the BO fluctuations that are abundant above T_{BO} in kagome metals [49, 50]. The sizable off-site Umklapp scattering by the BO fluctuations induces the odd-parity and TRSB current order. (=imaginary δt_{ij}^c). This cLC mechanism is universal because it is irrelevant to the origin of the BO. Furthermore, we discover that the coexistence of the BO and the cLC order gives rise to the novel Z_3 nematicity along the three lattice directions reported in Refs. [5, 19, 27]. The present theory reveals the close relationship between the cLC, BO, nematicity and

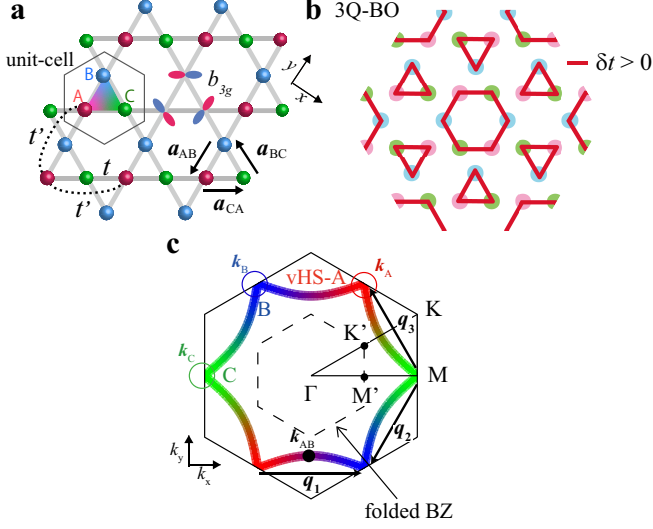


FIG. 1: **Lattice structure, Fermi surface, and BO form factor in kagome metal.** **a.** Kagome-lattice structure composed of the sublattices A, B and C. $2\mathbf{a}_{lm}$ is the minimum translation vector, and we set $|2\mathbf{a}_{lm}| = 1$. The relation $\mathbf{a}_{AB} + \mathbf{a}_{BC} + \mathbf{a}_{CA} = \mathbf{0}$ holds. **b.** 3Q Tri-Hexagonal bond order (BO) state. **c.** Fermi surface (FS) at $n = 0.917$ with the nesting vectors $\mathbf{q}_1, \mathbf{q}_2, \mathbf{q}_3$. The color of the FS represents the weight of the sublattice (A = red, B = blue, C = green). The FS has single sublattice character near the van-Hove singularity (vHS) points. In kagome metals, \mathbf{q}_1 connects vHS-A and vHS-B. It is given as $\mathbf{q}_1 = (2\mathbf{a}_{AB}) \times (2\pi/\sqrt{3})\mathbf{e}_z$, where \mathbf{e}_z is the unit vector perpendicular to the xy -plane.

SC state, which is significant to understand the unsolved quantum phase transitions in kagome metals.

The phase transitions in metals are described as the symmetry breaking of the normal self-energy; $\Delta\Sigma \equiv \Sigma - \Sigma_{A_1g}$ [45, 51]. $\Delta\Sigma$ is determined by the stationary condition of the free energy; $\delta F[\Delta\Sigma]/\delta(\Delta\Sigma) = 0$. The DW equation enables us to derive the solution that satisfies the stationary condition, as we proved based on the Luttinger-Ward theory [51]. Based on the DW equation, we discover that the odd-parity and TRSB $\Delta\Sigma$ is driven by the BO fluctuation exchange processes. (Note that the DW equation for $\Delta\Sigma$ is analogous to the Eliashberg equation for the SC gap Δ .)

Results

BO form factor and fluctuations.

Here, we introduce the kagome-lattice tight-binding model with a single d -orbital of each vanadium site (A, B, or C) shown in Fig. 1 a. (The d -orbital belongs to b_{3g} of the D_{2h} point group at V site, while its representation is not essential here.) The kinetic term is given by $\hat{H}_0 = \sum_{\mathbf{k}, l, m, \sigma} h_{lm}^0(\mathbf{k}) c_{\mathbf{k}, l, \sigma}^\dagger c_{\mathbf{k}, m, \sigma}$, where l, m denote the

sublattices A, B, C, and $h_{lm}^0(\mathbf{k}) (= h_{ml}^0(\mathbf{k})^*)$ is the Fourier transform of the nearest-neighbor hopping integral t in Ref. [52] in addition to the inter-sublattice hopping t' shown in Fig. 1 a. We set $t (= -0.5\text{eV})$ to fit the bandwidth, and $t' (= -0.08\text{eV})$ to reproduce the shape of the Fermi surface (FS). Numerical results are insensitive to the presence of t' . Hereafter, the unit of energy is eV unless otherwise noted. The FS around the van-Hove singularity (vHS) point ($\mathbf{k} \approx \mathbf{k}_A, \mathbf{k}_B$, or \mathbf{k}_C) is composed of a single $3d$ -orbital on V ion, which is called the sublattice interference [6]. This simple three-site model well captures the main pure-type FS in kagome metals [4, 53–57]. The FS at the vHS filling ($n_{\text{vHS}} = 0.917$ per site and both spins) is shown in Fig. 1 c. The wavevectors of the BO correspond to the inter-sublattice nesting vectors \mathbf{q}_n ($n = 1, 2, 3$) in Fig. 1 c. (The equivalent square lattice kagome model is convenient for the numerical study; see Supplementary Note 1.) The good inter-sublattice nesting of the FS naturally triggers the observed inter-sublattice BO at $\mathbf{q} = \mathbf{q}_n$, as shown in previous theoretical studies [6, 7, 12].

The Fourier transform of the BO modulation, δt_{ij}^b , gives the even-parity BO form factor $g_{\mathbf{q}}^{lm}(\mathbf{k})$ [45, 58]:

$$g_{\mathbf{q}}^{lm}(\mathbf{k}) = \frac{1}{N} \sum_i^{\text{sub-l}} \sum_j^{\text{sub-m}} \delta t_{ij}^b e^{i\mathbf{k} \cdot (\mathbf{r}_i - \mathbf{r}_j)} e^{-i\mathbf{q} \cdot \mathbf{r}_j}, \quad (1)$$

where \mathbf{q} is the wavevector of the BO. In this study, we use the simplified BO form factor due to the nearest sites presented in Supplementary Note 2-1. The form factor at $\mathbf{q} = \mathbf{q}_1$, $g_{\mathbf{q}_1}^{lm}$, is nonzero only when $\{l, m\} = \{A, B\}$, and we set $g_{\mathbf{q}}^{lm} = g_{\mathbf{q}_1}^{lm}$ when \mathbf{q} is in region I in Fig. 2 b. In the same way, we set $g_{\mathbf{q}}^{lm} = g_{\mathbf{q}_2}^{lm} (g_{\mathbf{q}_3}^{lm})$ when \mathbf{q} is in region II (III). $g_{\mathbf{q}_2}^{lm} (g_{\mathbf{q}_3}^{lm})$ is nonzero for $\{l, m\} = \{B, C\} (\{C, A\})$. This treatment is justified because the BO fluctuations strongly develop only for $\mathbf{q} \approx \mathbf{q}_n$ in kagome metals. Furthermore, we use $\bar{f}_{\mathbf{q}}(\mathbf{k}) = (f_{\mathbf{q}_n}(\mathbf{k}) + f_{\mathbf{q}_n}(\mathbf{k} + \mathbf{q} - \mathbf{q}_n))/2$ for $\mathbf{q} \sim \mathbf{q}_n$ in the numerical study to improve the accuracy. Both BO and cLC form factors are Hermite $\delta t_{ij}^{lm} = (\delta t_{ji}^{ml})^*$, which leads to the relation $g_{\mathbf{q}}^{lm}(\mathbf{k}) = (g_{-\mathbf{q}}^{ml}(\mathbf{k} + \mathbf{q}))^*$ [45].

To express the development of the bond order and fluctuations in kagome metals, we introduce the following effective BO interaction:

$$\hat{H}_{\text{int}} = -\frac{1}{N} \sum_{\mathbf{q}} \frac{v}{2} \hat{O}_{\mathbf{q}}^g \hat{O}_{-\mathbf{q}}^g, \quad (2)$$

where $\hat{O}_{\mathbf{q}}^g \equiv \sum_{\mathbf{k}, l, m, \sigma} g_{\mathbf{q}}^{lm}(\mathbf{k}) c_{\mathbf{k}+\mathbf{q}, l, \sigma}^\dagger c_{\mathbf{k}, m, \sigma}$ is the BO operator [45, 58, 59], and v is the effective interaction. We assume that the form factor $g_{\mathbf{q}}^{lm}(\mathbf{k})$ is normalized as $\max_{\mathbf{k}, l, m} |g_{\mathbf{q}}^{lm}(\mathbf{k})| = 1$ at each \mathbf{q} , i.e., $|\delta t_{ij}^b| \equiv 1/2$ for the nearest sites. Then, the maximum matrix element of BO interaction in Eq. (2) is $v/2$. The interaction (2) would originate from the combination of (i) the paramagnon-interference due to on-site U [12], (ii) the bond-stretching

phonon [60], and (iii) the Fock term of off-site Coulomb interaction V [9]. In (i), Eq. (2) is induced by the spin-fluctuation-mediated beyond-RPA processes, whose diagrammatic expressions are shown in Figs. 3 (c) and (d) in Ref. [12]. This processes give rise to the nematic BO in Fe-based SCs [45]. A great advantage of this theory [12] is that the function of the BO form factor and the BO wavevector are automatically optimized to maximize T_{BO} . Based on this theory, the BO at $\mathbf{q} = \mathbf{q}_n$ ($n = 1, 2, 3$) is robustly obtained based on the first principles multi-orbital model for CsV_3Sb_5 [12]. The effective parameter v in Eq. (2) is given as $v_{\text{AL}} \sim [g_{\text{back}} + g_{\text{um}}]/2$, which is about 1.5 near the BO critical point ($\lambda_{\text{bond}} \lesssim 1$), as we see in Fig. 3 (e) of Ref. [12]. Thus, the value of v given by the AL processes is comparable to that used in the present study. In (ii), $g_{\mathbf{q}}^{lm}(\mathbf{k})$ is given by the hopping modulation due to the stretching mode and $v = 2\eta^2/\omega_{\text{D}}$, where η is the electron-phonon (e-ph) coupling constant and ω_{D} is the phonon energy at $\mathbf{q} \approx \mathbf{q}_n$. The BO interaction for the three vHS points model was derived in Ref. [10]. In (iii), $v = 2V$ as we explain in the Supplementary Note 2-2. Thus, the effective interaction (2) is general. A possible driving forces of the BO have been discussed experimentally [61, 62].

Next, we study the susceptibility of the BO operator (per spin) defined as

$$\chi_g(\mathbf{q}, \omega_l) \equiv \frac{1}{2} \int_0^\beta d\tau \langle \hat{O}_{\mathbf{q}}^g(\tau) \hat{O}_{-\mathbf{q}}^g(0) \rangle e^{i\omega_l \tau} \quad (3)$$

where ω_l is a boson Matsubara frequency. $\hat{O}_{\mathbf{q}}^g(\tau)$ is the Heisenberg representation of the BO operator. When $v = 0$, $\chi_g(q)$ is equivalent to the BO irreducible susceptibility $\chi_g^0(q)$ [45, 58]:

$$\chi_g^0(q) = \sum_{lmm'l'} \chi_g^{0, lmm'l'}(q), \quad (4)$$

$$\begin{aligned} \chi_g^{0, lmm'l'}(\mathbf{q}, \omega_l) &= \frac{T}{N} \sum_{\mathbf{k}, \epsilon_n} g_{\mathbf{q}}^{lm}(\mathbf{k})^* G_{lm'}(\mathbf{k} + \mathbf{q}, \epsilon_n + \omega_l) \\ &\quad \times G_{l'm}(\mathbf{k}, \epsilon_n) g_{\mathbf{q}}^{m'l'}(\mathbf{k}), \end{aligned} \quad (5)$$

where $q \equiv (\mathbf{q}, \omega_l = 2\pi Tl)$ and ϵ_n is a fermion Matsubara frequency. Equation (5) contains two form factors, so it vanishes when $l = m$ or $l' = m'$. Its diagrammatic expression is given in Fig. 2 a. The numerical result for $\chi_g^{0, \text{ABAB}}(\mathbf{q}, 0)$ is shown in Fig. 2 b, which exhibits the broad peak at the nesting vector between vHS-A and vHS-B; $\mathbf{q} = \mathbf{q}_1$.

The BO susceptibility in Eq. (3) is strongly magnified by the Hartree term of Eq. (2) because of the same form factors in both equations. Its process is expressed in Fig. 2 c, and its analytic expression is

$$\chi_g(q) = \chi_g^0(q)/(1 - v\chi_g^0(q)). \quad (6)$$

where the notation $q \equiv (\mathbf{q}, \omega_l = 2\pi Tl)$ is used. Here, the relation $\chi_g(\mathbf{q}_n, 0) \propto (1 - \alpha_{\text{BO}})^{-1}$ holds, where $\alpha_{\text{BO}} \equiv$

$\max_{\mathbf{q}} v\chi_g^0(\mathbf{q})$ is the BO stoner factor. $\chi_g(\mathbf{q}_n, 0)$ diverges when $\alpha_{\text{BO}} = 1$. In contrast, the cLC susceptibility for the odd-parity cLC form factor, $f_{\mathbf{q}}^{lm}(\mathbf{k} - \mathbf{q}/2) = -f_{\mathbf{q}}^{ml}(-\mathbf{k} - \mathbf{q}/2)$, is unchanged by the Hartree term because g is even-parity.

The BO susceptibility is the largest in the Hartree-Fock (HF) approximation. As we discuss in the Supplementary Note 3, the BO and cLC susceptibilities at $\mathbf{q} = \mathbf{q}_n$ are $\tilde{\chi}_g \propto (1 - (v + v')\chi_g^0)^{-1}$ and $\tilde{\chi}_{\text{cLC}} \propto (1 - v''\chi_g^0)^{-1}$, respectively. Here, $-v' \sim v'' \sim 0.3yv$ originates from the Fock term. (The coefficient y ($\sim O(1)$) depends on the origin of BO fluctuations. $y = 1/2$ for H_{int} in Eq. (2). The detailed discussion on y will be presented later.) Thus, both susceptibilities are enlarged, while $\tilde{\chi}_{\text{cLC}} < \tilde{\chi}_g$ within the HF approximation. However, we discover that $-v'$ and v'' are further enlarged by the Maki-Thompson (MT) vertex corrections.

The MT term describes the scattering of electrons due to the developed bosonic fluctuations. This scattering process is important in metals near the quantum critical points. For example, in nearly antiferromagnetic metals, the d -wave SC transition is induced by the MT processes of spin fluctuations. In kagome metals, the MT term represents the strong inter vHS scattering of electrons mediated by the abundant BO fluctuations; see Fig. 3 a. (The MT term also describes the s -wave SC state in kagome metals [12].) Here, we find that both $\tilde{\chi}_g$ and $\tilde{\chi}_{\text{cLC}}$ are comparably enlarged due to the MT processes in the present theory.

To understand the BO+cLC phase diagram and the energy scale of these orders accurately, we have to include the self-energy that describes the quasiparticle properties. We calculate the on-site self-energy due to BO fluctuations (see Eq. (8) in Methods). The fluctuation-induced self-energy is essential to reproduce the T -dependence of various physical quantities, as well-known in spin fluctuation theories [63–65]. Here, we calculate $\chi_g(q)$ in Eq. (6) and $\Sigma_m(\epsilon_n)$ in Eq. (8) self-consistently.

BO fluctuation-mediated cLC order.

Next, we discuss the cLC mechanism. The HF approximation for the BO interaction (2) does not lead to the cLC order, as we explain in the Supplementary Note 3. (It is the same for off-site Coulomb interaction case; see Supplementary Note 2-1.) Thus, the cLC order should be ascribed to the beyond-HF mechanism. Here, we explain that the strong electron scattering between different vHS points due to the BO fluctuations, which are described as the MT processes, causes the odd-parity cLC order $\delta t_{ij}^c = -\delta t_{ji}^c$. (Note that the spin-fluctuation-exchange processes cause the cLC order in quasi-1D systems [66].) This process is generated by solving the following lin-

earized DW equation [41, 51, 66]:

$$\lambda_{\mathbf{q}} f_{\mathbf{q}}^L(k) = \frac{T}{N} \sum_{p, M_1, M_2} I_{\mathbf{q}}^{L, M_1}(k, p) \times \{-G(p)G(p+\mathbf{q})\}^{M_1, M_2} f_{\mathbf{q}}^{M_2}(p), \quad (7)$$

where $L \equiv (l, l')$ and M_i represent the pair of sublattice indices. $I_{\mathbf{q}}^{L, M}(k, p) \propto -\chi_g(k-p)$ is given by the BO fluctuation scattering process shown in Fig. 3 a, which is called the MT process. The expression of $I_{\mathbf{q}}^{L, M}$ is given in Eq. (10) in Methods section. Note that $T \sum_n \{-G(\mathbf{p}, \epsilon_n)G(\mathbf{p}+\mathbf{q}, \epsilon_n)\} > 0$.

By solving the DW equation (7), the optimized order parameter function is given as the eigenfunction $f_{\mathbf{q}}^L(k)$ for the maximum eigenvalue $\lambda_{\mathbf{q}}$. $\max_{\mathbf{q}}\{\lambda_{\mathbf{q}}\} = 1$ at the phase transition temperature. Note that $f_{\mathbf{q}}^L(k)$ represents the symmetry-breaking part in the normal self-energy $\Delta\Sigma(\mathbf{k}, \mathbf{q}) \sim \langle c_{\mathbf{k}+\mathbf{q}\sigma}^\dagger c_{\mathbf{k}\sigma} \rangle$, and DW equation is directly derived from the stationary condition $\delta F[\Delta\Sigma]/\delta(\Delta\Sigma) = 0$ [51]. We can regard the DW equation (7) as the gap equation for the optimized particle-hole (p-h) condensation [45, 51].

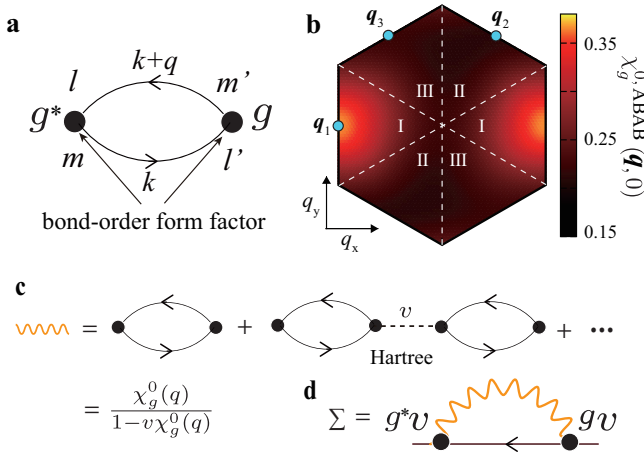


FIG. 2: **BO fluctuations and self-energy.** **a.** Expressions of the bond-order (BO) irreducible susceptibility $\chi_g^{0,lmml'}(q)$. **b.** Obtained \mathbf{q} -dependence for $\chi_g^{0,ABAB}(q)$, which takes the maximum at $\mathbf{q} = \mathbf{q}_1$. **c.** $\hat{\chi}_g(q)$ enlarged by the Hartree term of the electron-phonon interaction (2). [Note that $\hat{\chi}_g(q)$ is also enlarged by the Fock term of the off-site Coulomb interaction; see Supplementary Note 2-2.] **d.** Self-energy induced by the BO fluctuations.

Note that the BO fluctuation-mediated interaction for the self-energy (Eq. (8)) and that for the kernel function (Eq. (10)) have the same coefficient y , guaranteed by the Ward identity. The y depends on the BO fluctuation mechanism: $y = 1/2$ for the BO interaction v in Eq. (2) that works only in charge-channel. $y \approx 1/2$ for the AL mechanism for the same reason [12]. $y = 2$ for the off-site V that induced both charge- and three spin-channel BO fluctuations as we explain in Supplementary Note 2-2. In kagome metals, both v and V coexist. In this

case, BO fluctuations in charge-channel dominate over those in spin-channel, and therefore $y \gtrsim 0.5$ is expected in real kagome metals. Detailed explanation is given in Supplementary Note 2-3. Because we are interested in a general argument, we set $y = 0.5 \sim 1$ as a model parameter below. Note that the Aslaozov-Larkin term is unimportant as we discuss in Supplementary Note 4.

Figure 3 b shows the largest eigenvalue of the DW equation $\lambda_{\mathbf{q}}$ (red line) and BO Stoner factor $\alpha_{\mathbf{q}}^{\text{BO}} \equiv v\chi_g^0(\mathbf{q})$ (blue line) as functions of \mathbf{q} , for $v = 0.7$ and $T = 0.012$. They exhibit the maximum value at $\mathbf{q} = \mathbf{q}_n$ ($n = 1, 2, 3$). The corresponding solution of the DW equation is odd-parity: $f_{\mathbf{q}}^{lm}(\mathbf{k}-\mathbf{q}/2) = -f_{\mathbf{q}}^{ml}(-\mathbf{k}-\mathbf{q}/2)$. Then, the corresponding real-space hopping modulation is odd-parity $\delta t_{ij}^c = -\delta t_{ji}^c$ and pure imaginary when δt_{ij}^c is Hermitian. The obtained $\delta t_{AC}^c(R) \equiv \delta t_{iAJC}^c$ for the cLC at $\mathbf{q} = \mathbf{q}_3$ along the A-C direction is shown in Fig. 3 c, where the odd integer R is defined as $\mathbf{r}_i^C - \mathbf{r}_j^A \equiv R\mathbf{a}$. In addition, the odd-parity relation $\delta t_{AC}^c(R) = -\delta t_{CA}^c(-R)$ is verified. The obtained charge loop current pattern for the $3Q$ state is depicted in Fig. 3 d.

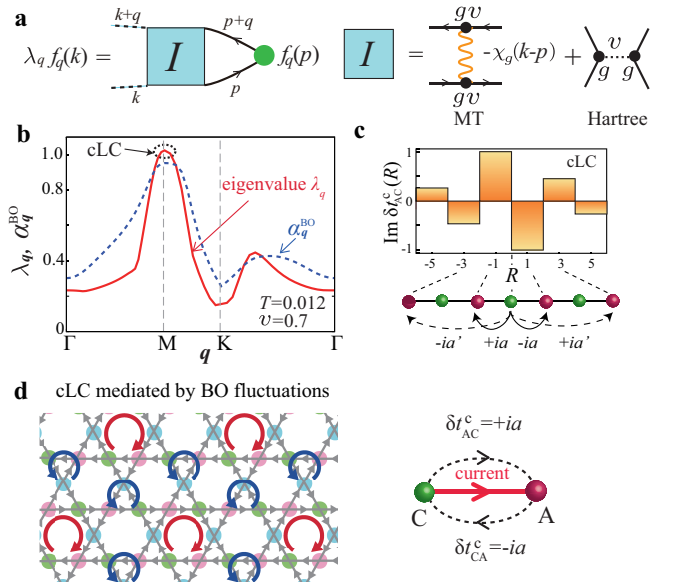


FIG. 3: **cLC order driven by BO fluctuation mechanism.** **a.** Density-wave (DW) equation due to the single exchange term of the bond-order (BO) fluctuations. **b.** Eigenvalue of the DW equation $\lambda_{\mathbf{q}}$ (red-solid line) and BO Stoner factor $\alpha_{\mathbf{q}}^{\text{BO}}$ (blue-dashed line) for $v = 0.7$ and $T = 0.012$. Both show peaks at $\mathbf{q} = \mathbf{q}_n$. **c.** Imaginary hopping modulation $\text{Im} \delta t_{AC}^c(R)$. Its triple- \mathbf{q} order gives the cLC pattern in **d.** One can check that the clock-wise (anti-clock-wise) loop currents on hexagons (triangles) in **d** are inverted and moved by \mathbf{a}_{AC} under the sign change of $f_{\mathbf{q}_3}^{\text{AC}}$.

Here, we discuss why the cLC order is mediated by the BO fluctuations. Let us consider the infinite series of MT terms in Fig. 4 a, which is equal to $f_{\mathbf{q}_3}^{\text{AC}}(\lambda_{\mathbf{q}_3}^{-1} - 1)^{-1}$ according to the DW equation (7). The first term together with other odd-order MT terms in Fig. 4 a give the repul-

sive Umklapp interaction, $\Gamma_{\text{um}}^{\text{MT}} < 0$, which leads to the odd-parity order $f_{\mathbf{q}_3}^{\text{AC}} = -f_{\mathbf{q}_3}^{\text{CA}}$. In contrast, the second term together with other even-order MT terms give the attractive backward interaction, $\Gamma_{\text{back}}^{\text{MT}} > 0$, which gives the attraction among the same $f_{\mathbf{q}_3}^{\text{lm}}$. Therefore, all series of MT terms cooperatively induce the odd-parity current order form factor shown in Fig. 3 c. Figure 4 b exhibits the obtained v -dependence of the cLC eigenvalue as a function of T in the case of $y = 1$.

Figure 4 c exhibits the T -dependence of $\lambda_{\mathbf{q}_3}$ for $v = 0.4 - 1.4$ at $y = 1$. The cLC transition temperature T_{cLC} is given by the relation $\lambda_{\mathbf{q}_3} = 1$. The color on each line represents α_{BO} : It is clearly seen that α_{BO} at $T = T_{\text{cLC}}$ monotonically increases with v . In 2D systems, α_{BO} asymptotically approaches 1 with v , but never exceeds 1 due to the χ_g -induced self-energy [65, 67]. Here, T_{BO} is defined as $\alpha_{\text{BO}} = \alpha_{\text{BO}}^*$ with $\alpha_{\text{BO}}^* = 0.985$, which is shown as a small circle on each line in Fig. 4 c, by considering the small inter-layer BO coupling $|v_{\perp}|$ ($\ll v$). (Overall results are unchanged for $\alpha_{\text{BO}}^* \sim 0.99$.) The three-dimensional (3D) BO appears when $\chi_g^{\text{3D}} = \chi_g^{\text{2D}} / (1 - |v_{\perp}| \chi_g^{\text{2D}}) = \infty$, that is, $|v_{\perp}| \sim (1 - \alpha_{\text{BO}})v$. Similar method is frequently used in deriving T_{SDW} in spin fluctuation theories [67]. When v is small, the relation $T_{\text{cLC}} > T_{\text{BO}}$ holds, which is natural because the MT term becomes large for $\alpha_{\text{BO}} \lesssim 1$. With increasing v , however, the opposite relation $T_{\text{cLC}} < T_{\text{BO}}$ is realized due to the large self-energy effect.

The obtained T_{cLC} and T_{BO} as functions of v are shown in Figs. 4 d $y = 1$ and e $y = 0.5$. In d, $T_{\text{cLC}} = T_{\text{BO}}$ is realized at $v = v^* \approx 1.03$, and $T_{\text{cLC}}/T_{\text{BO}} > 1$ is realized in the weak-coupling region $v < v^*$. The opposite relation $T_{\text{cLC}}/T_{\text{BO}} < 1$ is obtained in the strong-coupling region $v > v^*$ because the eigenvalue of DW equation (7) is suppressed by the large self-energy. In e, $T_{\text{cLC}} = T_{\text{BO}}$ at $v = v^* \approx 0.55$.

Figures 4 d and e indicate that both BO and cLC instabilities are comparable for $v^* \approx v$. Based on the parity argument, the BO (cLC) instability is given by $\Gamma_{\text{back}} + (-)\Gamma_{\text{um}}$. Therefore, the relation $\Gamma_{\text{back}} \gg |\Gamma_{\text{um}}|$ should be satisfied for $v^* \approx v$. In fact, the Hartree process gives positive $\Gamma_{\text{back}}^{\text{H}} = \Gamma_{\text{um}}^{\text{H}} \sim v / (1 - v\chi_g^0)$, so the Hartree and MT processes strengthen each other in Γ_{back} but cancel each other in Γ_{um} . This relation is verified by the parquet RG study in Supplementary Note 5.

We discuss that Figs. 4 d and e naturally explain the experimental P - T phase diagram with T_{BO} and T_2^* ($\sim T_{\text{TRSB}}$) given by μSR study [15] for $A=\text{Rb}$, considering that v/W_{band} decreases with P . A schematic BO+cLC phase diagram derived from the present theory is depicted in Fig. 4 f. (This schematic phase diagram is supported by the Ginzburg-Landau (GL) analysis in Supplemental Figs. 11 a-c.) The suppression of the secondary order due to the primary order is considered.) The cLC phase is realized next to the BO phase because it is mediated by the BO fluctuations. This cLC+BO phase

diagram is reminiscent of the SC-SDW phase diagram of spin-fluctuation-mediated superconductors, which has been reproduced by considering the self-energy [67].

Z_3 -nematic state given by the cLC-BO coexistence.

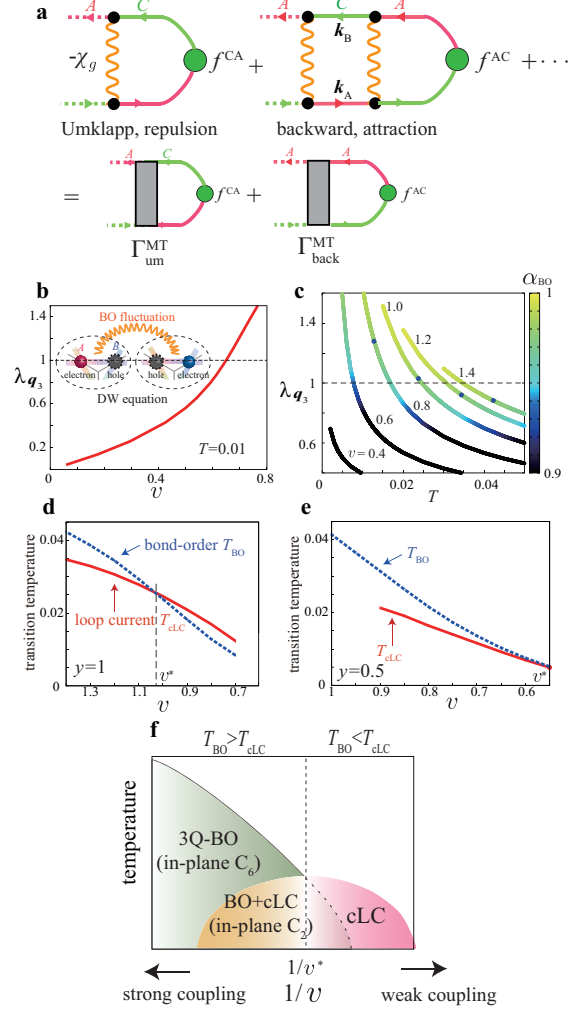


FIG. 4: cLC and BO transition temperatures and predicted phase diagram. **a.** Series of Maki-Thompson (MT) processes produced in the density-wave (DW) equation. Yellow wavy lines represent the bond order (BO) propagators. The first-order and other odd-order terms give the repulsive Umklapp scattering $\Gamma_{\text{um}}^{\text{MT}} < 0$. The second-order and other even-order terms give the attractive backward scattering $\Gamma_{\text{back}}^{\text{MT}} > 0$. Both scatterings give the odd-parity charge loop current (cLC) order cooperatively. **b.** Obtained v -dependence of the eigenvalue of cLC $\lambda_{\mathbf{q}_3}$ at $y = 1$. **c.** Obtained T -dependence of $\lambda_{\mathbf{q}_3}$ at $y = 1$. α_{BO} is shown by the color of each line, and the small black circle on each line represents T_{BO} . The relation $T_{\text{cLC}} > T_{\text{BO}}$ is satisfied in the weak-coupling region ($v < v^*$). **d.** Obtained T_{cLC} and T_{BO} as functions of v for $y = 1$ and **e.** $y = 0.5$. **f.** Schematic phase diagram in the present theory. The nematic 3Q BO+cLC coexisting phase appears when $T_{\text{cLC}} < T_{\text{BO}}$.

To understand the cLC+BO coexisting states in Fig. 4 f, the Ginzburg-Landau (GL) free energy analysis is very useful [10, 30, 31]. For example, the third-order GL term is $F^{(3)} = b_1\phi_1\phi_2\phi_3 + b_2(\phi_1\eta_2\eta_3 + \eta_1\phi_2\eta_3 + \eta_1\eta_2\phi_3)$, where the coefficients satisfy the relation $b_1 \sim -b_2$, and $(\phi_1, \phi_2, \phi_3) [(\eta_1, \eta_2, \eta_3)]$ is the magnitude of the BO [cLC] parameter at $\mathbf{q} = \mathbf{q}_1, \mathbf{q}_2, \mathbf{q}_3$. Here, we introduce the 3Q states $\phi_1 = (\phi/\sqrt{3})(1, 1, 1)$, $\eta_1 = (\eta/\sqrt{3})(1, 1, 1)$, and $\eta_2 = (\eta/\sqrt{3})(1, -1, -1)$. The chiral center of η_1 coincides with the center of the BO ϕ_1 , while the center of η_2 is shifted by \mathbf{a}_{BA} from that of ϕ_1 . Thus, the coexisting state $(\phi_1, \eta_{1[2]})$ has the $C_{6[2]}$ -symmetry as shown in Fig. 5 a [c], and its FS in the folded Brillouin zone is in Fig. 5 b [d]. As we explain in Supplementary Note 6-1, $F^{(3)}$ for the C_2 -coexisting state is lower than that for the C_6 -coexisting state in the case of $|\phi| \gg |\eta|$ for fixed $|\phi|, |\eta|$. (The optimized cLC order in the C_2 -phase is $\eta'_2 \propto (2, -1, -1)$; see Supplementary Note 6-1.) Therefore, the BO+cLC Z_3 nematic state is realized when $v > v^*$. This result is consistent with the recent observation of out-of-phase combination of bond charge order and loop currents by STM measurement [68]. We comment that the nematic BO+cLC phase is obtained when $T_{BO} \gtrsim T_{cLC}$ by minimizing the GL free energy $F[\phi, \eta]$ exactly in Supplementary Note 6-2.

We also discuss the case of $v < v^*$, where cLC is the primary order as shown in Fig. 4 f. The C_6 symmetry 3Q cLC order appears at $T = T_{cLC}$ when $2d_{2,a}/d_{2,b} > 1$ as we discuss in Supplementary Note 5, where $d_{2,a}$ ($d_{2,b}$) is the GL coefficients of the η_1^4 ($\eta_1^2\eta_2^2$) term. Note that the primary 3Q cLC order induces the secondary BO parameter even above T_{BO} through the b_2 -term in $F^{(3)}$ [10]. In contrast, the 1Q cLC state is realized when $2d_{2,a}/d_{2,b}$ is smaller than unity. Thus, the electronic state becomes nematic at T_{cLC} ($> T_{BO}$). In this case, there is no secondary BO component above T_{BO} . Recently, strong evidence of the emergence of the 1Q cLC state at $\sim 130\text{K}$ ($> T_{BO}$) has been reported by the magnetic torque measurement [21].

The obtained nematic BO+cLC state is TRSB and two-dimensional. Other possible nematic state is the shift-stacking of the 3Q BO layers, each of which has C_6 symmetry. The shift-stacking is caused by the 3Q state composed of the 3D BO at \mathbf{q}_n^{3D} with $q_{1,z}^{3D} = q_{2,z}^{3D} = \pi$ and $q_{3,z}^{3D} = 0$ [10]. We stress that these two different nematic states can be realized at different temperatures.

Giant AHE in cLC+BO state.

Next, we discuss the transport phenomena that originate from the cLC [24, 69]. Using the general expression of the intrinsic conductivity [65, 71], we calculate the Hall conductivity (σ_{xy} and σ_{yx}) due to the Fermi-surface contribution in the BO+cLC state. The expression is $\sigma_{\mu\nu} = \frac{1}{N} \sum_{\mathbf{k}} A_{\mu\nu}(\mathbf{k})$, where $A_{\mu\nu}(\mathbf{k}) = \frac{e^2}{\hbar} \frac{1}{\pi} \text{Tr}\{\hat{v}_{\mathbf{k},\mu} \hat{G}_{\mathbf{k}}(i\gamma) \hat{v}_{\mathbf{k},\nu} \hat{G}_{\mathbf{k}}(-i\gamma)\}$. Here, $\hat{G}_{\mathbf{k}}(\epsilon) = ((\epsilon +$

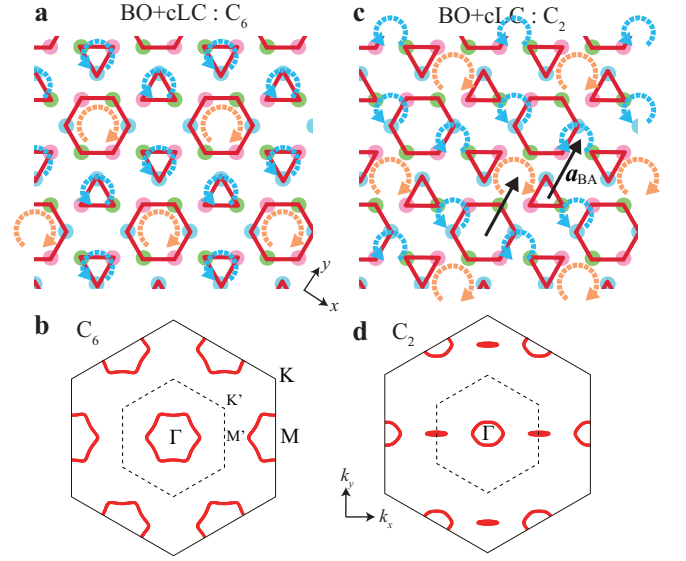


FIG. 5: **cLC+BO coexisting states with C_6 and C_2 symmetries.** **a.** C_6 -symmetric bond order (BO) and charge loop current (cLC) coexisting state in real space. **b.** Its folded Fermi surface (FS). The folded Brillouin zone is shown by dotted lines. **c.** C_2 -symmetric BO+cLC coexisting state. The nematicity originates from the out-of-phase combination of bond and current orders. **d.** Its nematic FS. Here, the director is parallel to \mathbf{a}_{BA} because the cLC order in **c** is shifted by \mathbf{a}_{BA} from the cLC order in **a**. Thus, the Z_3 nematic state with different three directors is realized. Here, we use large $|\delta t_{ij}^{b,c}|$ ($= 0.05$) to exaggerate the nematicity.

$\mu)\hat{1} - \hat{h}_{\mathbf{k}})^{-1}$ is the Green function matrix, where $\hat{h}_{\mathbf{k}}$ is the 12×12 tight-binding model with the 3Q BO and cLC order, and $\hat{v}_{\mathbf{k},\mu} = d\hat{h}_{\mathbf{k}}/dk_{\mu}$ is the velocity operator. γ (> 0) is the electron damping rate that is given by the imaginary part of the self-energy. We set $n = n_{\text{vHS}}$ and $|\delta t_{ij}^b| = |\delta t_{ij}^c| = 0.025$, where the band hybridization gap due to the BO+cLC order is about $\Delta \approx 2\sqrt{|\delta t_{ij}^b|^2 + |\delta t_{ij}^c|^2} = 0.07$.

Figure 6 a shows the obtained conductivities in the nematic BO+cLC state, in the unit of $\frac{e^2}{h}$ ($= 2.4 \times 10^{-4} \Omega^{-1}$). When $\gamma \ll \Delta$, the Hall conductivity $\sigma_H \equiv \frac{1}{2}(\sigma_{xy} - \sigma_{yx})$ is almost constant, and its magnitude is proportional to $|\delta t_{ij}^c|$. When $\gamma \gg \Delta$, in contrast, σ_H decreases with γ in proportion to γ^{-2} . This crossover behavior is universal in the intrinsic Hall effect, which was first revealed in heavy fermion systems, and found to be universal in later studies [65, 70–72]. Note that $\frac{1}{2}(\sigma_{xy} + \sigma_{yx})$ is nonzero in the nematic state. To understand the origin of the intrinsic Hall effect, we plot $A_H(\mathbf{k}) \equiv (A_{xy}(\mathbf{k}) - A_{yx}(\mathbf{k}))/2$ at $\gamma = 0.05$ in Fig. 6 b: It shows a large positive value mainly around the vHS points, due to the band-hybridization induced by the cLC order. The obtained $\sigma_H \sim 1$ corresponds to $4 \times 10^3 \Omega^{-1} \text{cm}^{-1}$ because the interlayer spacing is $\sim 0.6 \text{nm}$. Thus, giant AHE $\sigma_H \sim 10^2 \Omega^{-1} \text{cm}^{-1}$ reported in Refs. [25, 26] is understood in this theory.

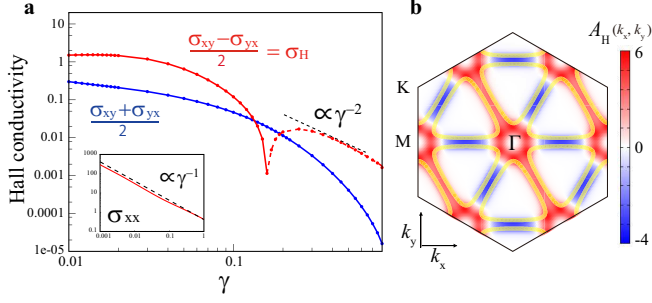


FIG. 6: **Giant AHE in nematic cLC+BO state.** **a.** Anomalous Hall conductivity in the nematic BO+cLC state ($|\delta t_{ij}^{b,c}| = 0.025$) as a function of the electron damping rate $\gamma \propto \tau^{-1}$. The full (broken) line represents the positive (negative) value. Thus, the Hall conductivity σ_H becomes large in the low-resistivity region ($\gamma \lesssim 0.03$). **b.** $A_H(\mathbf{k})$ at $\gamma = 0.05$: $\frac{1}{N} \sum_{\mathbf{k}} A_H(\mathbf{k}) = \sigma_H$.

Parquet RG theory, Field-induced cLC mechanism.

To verify the idea of the BO fluctuation-mediated cLC, we perform the analysis of the parquet renormalization group (RG) formulation [10, 73] and present the results in Supplementary Note 5. A great merit of the RG method is that both particle-particle and particle-hole channels are treated on the same footing. We find that both BO and cLC fluctuations cooperatively develop in Supplementary Fig. 6. This result of the RG study strongly supports the validity of the DW equation analysis.

We comment on the complementary relationship between the present theory and the parquet RG theory. The latter theory solves a simplified 3-patch model in an unbiased way, leading to the development of both cLC order and BO, while the relationship between the two orders is not clear. On the other hand, the present theory focuses on the existence of the experimental BO phase and reveals that abundant BO quantum fluctuations lead to TRSB particle-hole condensation. Thus, the concept of the BO fluctuation-mediated cLC has been verified based on different reliable theories.

Summary.

In summary, we proposed a cLC mechanism mediated by the BO fluctuations in kagome metals. This cLC mechanism is universal because it is independent of the origin of the BO. The validity of the idea of the BO fluctuation-mediated cLC has been confirmed by the parquet RG study in Supplementary Note 5. Furthermore, we revealed that novel Z_3 nematicity emerges under the coexistence of the cLC and the BO reported in Refs. [5, 19, 27] in addition to the giant AHE [25, 26]. This theory presents a promising scenario for understanding the BO, the cLC and the nematicity in kagome metals in a unified way.

In the present study, we focus on the pure-type band

composed of b_{3g} -orbital. However, the impact of other 3d-orbitals on the cLC order has also been studied in Refs. [30, 74]. The extension of the present theory to multi-orbital models is a very important future issue.

Here, we shortly discuss several experimental evidences of the BO+cLC coexistence. Recent transport measurement of highly symmetric fabricated CsV_3Sb_5 micro sample [75] reveals that small magnetic field h_z ($< 10\text{T}$) or small strain gives rise to the nematic BO+cLC coexisting state below T_{BO} . This finding is well explained by the recent GL theory under h_z [76]: The current-bond- h_z trilinear coupling caused by the orbital magnetization gives rise to the sizable h_z -induced cLC order in the BO state. This theory also explains h_z -induced enhancement of the cLC order observed by μSR measurements [15, 17, 18] and field-tuned chiral transport study [20]. It is noteworthy that the nematic electronic state that supports the C_2 BO+cLC order in Fig. 5 c has been reported by recent STM measurement [68].

Finally, we comment on some interesting kagome metals other than AV_3Sb_5 . Double-layer kagome metal ScV_6Sn_6 shows $\sqrt{3} \times \sqrt{3}$ charge-density wave (CDW) [77]. It was proposed that the CDW originates from the flat phonon modes with Sn vibrations [78, 79]. Interestingly, ScV_6Sn_6 also exhibits the spontaneous TRSB state [80]. The mechanism of the TRSB state in ScV_6Sn_6 is an interesting future problem. (Note that the existence of the vHS points is not a requirement for the cLC order [66].) The GL free energy analysis was performed in Ref. [81]. Recently, very weak but definite signal of the nematic electronic order has been observed in Ti-based kagome metal CsTi_3Bi_5 [82, 83]. To explain the observed hidden nematicity, the odd-parity BO without TRSB has been predicted theoretically [84].

Methods

Self-energy due to BO fluctuations.

To understand the BO+cLC phase diagram and the energy scale of these orders accurately, we have to include the self-energy that describes the quasiparticle properties. We calculate the on-site self-energy due to BO fluctuations as

$$\Sigma_m(\epsilon_n) = \frac{T}{N} \sum_{\mathbf{k}, q, m'', m'''} G_{m'm''}(\mathbf{k} + \mathbf{q}, \epsilon_n + \omega_l) \times B_{mm', m''m'}(k, q), \quad (8)$$

$$B_{mm', m''m'}(k, q) = g_{\mathbf{q}}^{m'm}(\mathbf{k}) g_{\mathbf{q}}^{m''m}(\mathbf{k})^* \cdot yv(1 + v\chi_g(q))$$

which is shown in Fig. 2 d. Then, the Green function is given as $\hat{G}(k) = (i\epsilon_n + \mu - \hat{h}(\mathbf{k}) - \hat{\Sigma}(\epsilon_n))^{-1}$. The effect of thermal fluctuations described by the self-energy is essential to reproduce the T -dependence of various physical quantities. Here, $y = 1/2$ when \hat{H}_{int} is given in

Eq. (2). In the present numerical study, we calculate $\chi_g(q) = \chi_g^0(q)/(1 - v\chi_g^0(q))$ and $\Sigma_m(\epsilon_n)$ in Eq. (8) self-consistently.

Kernel function of the DW equation.

The kernel function due to BO fluctuations in Eq. (7) is given as

$$I_{\mathbf{q}}^{ll',mm'}(k,p) = -g_{\mathbf{p}-\mathbf{k}}^{m'l'}(\mathbf{k})yv(1+v\chi_g(k-p))g_{\mathbf{k}-\mathbf{p}}^{lm}(\mathbf{p}+\mathbf{q}) + g_{\mathbf{q}}^{ll'}(\mathbf{k})vg_{\mathbf{q}}^{mm'}(\mathbf{p})^*, \quad (10)$$

which is expressed in Fig. 3 a and Supplementary Fig. 4 a. The first term, the MT term, is important when $\alpha_{\text{BO}} \lesssim 1$, and its first term is the Fock term. The second term, the Hartree term, vanishes when the eigenfunction $\hat{f}_{\mathbf{q}}(k)$ is orthogonal to the BO form factor $\hat{g}_{\mathbf{q}}(k)$, like the cLC order is. Note that $\hat{B}(k,q) = -\hat{I}_0(k,k+q)$. A more detailed discussion is presented in Supplementary Note 3.

Numerical Analysis. In this study, we solved the eigenvalue equation with the kernel function (7) and the integral equations (8) and (9) numerically, by dividing the Brillouin zone into 60×60 \mathbf{k} meshes. The number of \mathbf{k} meshes is fine enough to achieve reliable numerical accuracy ($\sim 1\%$) at the calculated temperatures ($T \sim 0.01$).

Acknowledgments

We are grateful to S. Onari, A. Ogawa, Y. Matsuda, T. Shibauchi, K. Hashimoto, and T. Asaba for fruitful discussions.

[1] B. R. Ortiz, L. C. Gomes, J. R. Morey, M. Winiarski, M. Bordelon, J. S. Mangum, I. W. H. Oswald, J. A. Rodriguez-Rivera, J. R. Neilson, S. D. Wilson, E. Ertekin, T. M. McQueen, and E. S. Toberer, *New kagome prototype materials: discovery of KV_3Sb_5 , RbV_3Sb_5 , and CsV_3Sb_5* , Phys. Rev. Materials **3**, 094407 (2019).

[2] B. R. Ortiz, S. M. L. Teicher, Y. Hu, J. L. Zuo, P. M. Sarte, E. C. Schueller, A. M. M. Abeykoon, M. J. Krogstad, S. Rosenkranz, R. Osborn, R. Seshadri, L. Balents, J. He, and S. D. Wilson, *CsV_3Sb_5 : A \mathbb{Z}_2 Topological Kagome Metal with a Superconducting Ground State*, Phys. Rev. Lett. **125**, 247002 (2020).

[3] F. H. Yu, D. H. Ma, W. Z. Zhuo, S. Q. Liu, X. K. Wen, B. Lei, J. J. Ying, and X. H. Chen, *Unusual competition of superconductivity and charge-density-wave state in a compressed topological kagome metal*, Nat. Commun. **12**, 3645 (2021).

[4] Y.-X. Jiang, J.-X. Yin, M. M. Denner, N. Shumiya, B. R. Ortiz, G. Xu, Z. Guguchia, J. He, M. S. Hossain, X. Liu, J. Ruff, L. Kautzsch, S. S. Zhang, G. Chang, I. Belopolski, Q. Zhang, T. A. Cochran, D. Multer, M. Litskevich,

Z.-J. Cheng, X. P. Yang, Z. Wang, R. Thomale, T. Neupert, S. D. Wilson, and M. Z. Hasan, *Unconventional chiral charge order in kagome superconductor KV_3Sb_5* , Nat. Mater. **20**, 1353 (2021).

[5] H. Li, H. Zhao, B. R. Ortiz, T. Park, M. Ye, L. Balents, Z. Wang, S. D. Wilson, and I. Zeljkovic, *Rotation symmetry breaking in the normal state of a kagome superconductor KV_3Sb_5* , Nat. Phys. **18**, 265 (2022).

[6] M. L. Kiesel, C. Platt, and R. Thomale, *Unconventional Fermi Surface Instabilities in the Kagome Hubbard Model*, Phys. Rev. Lett. **110**, 126405 (2013).

[7] W.-S. Wang, Z.-Z. Li, Y.-Y. Xiang, and Q.-H. Wang, *Competing electronic orders on kagome lattices at van Hove filling*, Phys. Rev. B **87**, 115135 (2013).

[8] X. Wu, T. Schwemmer, T. Müller, A. Consiglio, G. Sangiovanni, D. Di Sante, Y. Iqbal, W. Hanke, A. P. Schnyder, M. M. Denner, M. H. Fischer, T. Neupert, and R. Thomale, *Nature of Unconventional Pairing in the Kagome Superconductors AV_3Sb_5 ($A = K, Rb, Cs$)*, Phys. Rev. Lett. **127**, 177001 (2021).

[9] M. M. Denner, R. Thomale, and T. Neupert, *Analysis of Charge Order in the Kagome Metal AV_3Sb_5 ($A = K, Rb, Cs$)*, Phys. Rev. Lett. **127**, 217601 (2021).

[10] T. Park, M. Ye, and L. Balents, *Electronic instabilities of kagome metals: Saddle points and Landau theory*, Phys. Rev. B **104**, 035142 (2021).

[11] Y.-P. Lin and R. M. Nandkishore, *Complex charge density waves at Van Hove singularity on hexagonal lattices: Haldane-model phase diagram and potential realization in the kagome metals AV_3Sb_5 ($A = K, Rb, Cs$)*, Phys. Rev. B **104**, 045122 (2021).

[12] R. Tazai, Y. Yamakawa, S. Onari, and H. Kontani, *Mechanism of exotic density-wave and beyond-Migdal unconventional superconductivity in kagome metal AV_3Sb_5 ($A = K, Rb, Cs$)*, Sci. Adv. **8**, eabl4108 (2022).

[13] M. Roppongi, K. Ishihara, Y. Tanaka, K. Ogawa, K. Okada, S. Liu, K. Mukasa, Y. Mizukami, Y. Uwatoko, R. Grasset, M. Konczykowski, B. R. Ortiz, S. D. Wilson, K. Hashimoto, and T. Shibauchi, *Bulk evidence of anisotropic s-wave pairing with no sign change in the kagome superconductor CsV_3Sb_5* , Nat. Commun. **14**, 667 (2023).

[14] W. Zhang, X. Liu, L. Wang, C. Wai T., Z. Wang, S. T. Lam, W. Wang, J. Xie, X. Zhou, Y. Zhao, S. Wang, J. Tallon, K. T. Lai, and S. K. Goh, *Nodeless superconductivity in kagome metal CsV_3Sb_5 with and without time reversal symmetry breaking*, Nano Lett., **23**, 872 (2023).

[15] Z. Guguchia, C. Mielke III, D. Das, R. Gupta, J.-X. Yin, H. Liu, Q. Yin, M.H. Christensen, Z. Tu, C. Gong, N. Shumiya, Ts. Gamsakhurdashvili, M. Elender, Pengcheng Dai, A. Amato, Y. Shi, H.C. Lei, R.M. Fernandes, M.Z. Hasan, H. Luetkens, and R. Khasanov, *Tunable nodal kagome superconductivity in charge ordered RbV_3Sb_5* , Nat. Commun. **14**, 153 (2023).

[16] L. Yu, C. Wang, Y. Zhang, M. Sander, S. Ni, Z. Lu, S. Ma, Z. Wang, Z. Zhao, H. Chen, K. Jiang, Y. Zhang, H. Yang, F. Zhou, X. Dong, S. L. Johnson, M. J. Graf, J. Hu, H.-J. Gao, and Z. Zhao, *Evidence of a hidden flux phase in the topological kagome metal CsV_3Sb_5* , arXiv:2107.10714 (available at <https://arxiv.org/abs/2107.10714>).

[17] C. Mielke, D. Das, J.-X. Yin, H. Liu, R. Gupta, Y.-X. Jiang, M. Medarde, X. Wu, H. C. Lei, J. Chang, P. Dai, Q. Si, H. Miao, R. Thomale, T. Neupert, Y.

- Shi, R. Khasanov, M. Z. Hasan, H. Luetkens, and Z. Guguchia, *Time-reversal symmetry-breaking charge order in a kagome superconductor*, Nature **602**, 245 (2022).
- [18] R. Khasanov, D. Das, R. Gupta, C. Mielke, M. Elender, Q. Yin, Z. Tu, C. Gong, H. Lei, E. T. Ritz, R. M. Fernandes, T. Birol, Z. Guguchia, and H. Luetkens, *Time-reversal symmetry broken by charge order in CsV_3Sb_5* , Phys. Rev. Research **4**, 023244 (2022).
- [19] Y. Xu, Z. Ni, Y. Liu, B. R. Ortiz, S. D. Wilson, B. Yan, L. Balents, and L. Wu, *Universal three-state nematicity and magneto-optical Kerr effect in the charge density waves in AV_3Sb_5 ($A=\text{Cs}, \text{Rb}, \text{K}$)*, Nat. Phys. **18**, 1470 (2022).
- [20] C. Guo, C. Putzke, S. Konyzheva, X. Huang, M. Gutierrez-Amigo, I. Errea, D. Chen, M. G. Vergniory, C. Felser, M. H. Fischer, T. Neupert, and P. J. W. Moll, *Switchable chiral transport in charge-ordered Kagome metal CsV_3Sb_5* , Nature **611**, 461 (2022).
- [21] T. Asaba, A. Onishi, Y. Kageyama, T. Kiyosue, K. Ohtsuka, S. Suetsugu, Y. Kohsaka, T. Gaggli, Y. Kasahara, H. Murayama, K. Hashimoto, R. Tazai, H. Kontani, B. R. Ortiz, S. D. Wilson, Q. Li, H.-H. Wen, T. Shibauchi, and Y. Matsuda, *Evidence for an odd-parity nematic phase above the charge density wave transition in kagome metal CsV_3Sb_5* , arXiv:2309.16985 (available at <https://arxiv.org/abs/2309.16985>). (to be published in Nat. Phys.)
- [22] D. R. Saykin, C. Farhang, E. D. Kountz, D. Chen, B. R. Ortiz, C. Shekhar, C. Felser, S. D. Wilson, R. Thomale, J. Xia, and A. Kapitulnik, *High Resolution Polar Kerr Effect Studies of CsV_3Sb_5 : Tests for Time Reversal Symmetry Breaking Below the Charge Order Transition*, Phys. Rev. Lett. **131**, 016901 (2023).
- [23] Y. Xiang, Q. Li, Y. Li, W. Xie, H. Yang, Z. Wang, Y. Yao, and H.-H. Wen, *Twofold symmetry of c -axis resistivity in topological kagome superconductor CsV_3Sb_5 with in-plane rotating magnetic field*, Nat. Commun. **12**, 6727 (2021).
- [24] F. D. M. Haldane, *Model for a Quantum Hall Effect without Landau Levels: Condensed-Matter Realization of the "Parity Anomaly"*, Phys. Rev. Lett. **61**, 2015 (1988).
- [25] S.-Y. Yang, Y. Wang, B. R. Ortiz, D. Liu, J. Gayles, E. Derunova, R. Gonzalez-Hernandez, L. Šmejkal, Y. Chen, S. S. P. Parkin, S. D. Wilson, E. S. Toberer, T. McQueen, and M. N. Ali, *Giant, unconventional anomalous Hall effect in the metallic frustrated magnet candidate, KV_3Sb_5* , Sci. Adv. **6**, eabb6003 (2020).
- [26] F. H. Yu, T. Wu, Z. Y. Wang, B. Lei, W. Z. Zhuo, J. J. Ying, and X. H. Chen, *Concurrence of anomalous Hall effect and charge density wave in a superconducting topological kagome metal*, Phys. Rev. B **104**, L041103 (2021).
- [27] L. Nie, K. Sun, W. Ma, D. Song, L. Zheng, Z. Liang, P. Wu, F. Yu, J. Li, M. Shan, D. Zhao, S. Li, B. Kang, Z. Wu, Y. Zhou, K. Liu, Z. Xiang, J. Ying, Z. Wang, T. Wu, and X. Chen, *Charge-density-wave-driven electronic nematicity in a kagome superconductor*, Nature **604**, 59 (2022).
- [28] S. Ni, S. Ma, Y. Zhang, J. Yuan, H. Yang, Z. Lu, N. Wang, J. Sun, Z. Zhao, D. Li, S. Liu, H. Zhang, H. Chen, K. Jin, J. Cheng, L. Yu, F. Zhou, X. Dong, J. Hu, H.-J. Gao, and Z. Zhao, *Anisotropic Superconducting Properties of Kagome Metal CsV_3Sb_5* , Chin. Phys. Lett. **38**, 057403 (2021).
- [29] J.-Wei D., Z. Wang, S. Zhou, *Loop-current charge density wave driven by long-range Coulomb repulsion on the kagome lattice*, Phys. Rev. B **107**, 045127 (2023).
- [30] M. H. Christensen, T. Birol, B. M. Andersen, R. M. Fernandes, *Loop currents in AV_3Sb_5 kagome metals: multipolar and toroidal magnetic orders*, Phys. Rev. B **106**, 144504 (2022).
- [31] F. Grandi, A. Consiglio, M. A. Sentef, R. Thomale, D. M. Kennes, *Theory of nematic charge orders in kagome metals*, Phys. Rev. B **107**, 155131 (2023).
- [32] C. M. Varma, *Non-Fermi-liquid states and pairing instability of a general model of copper oxide metals*, Phys. Rev. B **55**, 14554 (1997).
- [33] A. A. Nersesyan, G. I. Japaridze, and I. G. Kimeridze, *Low-temperature magnetic properties of a two-dimensional spin nematic state*, J. Phys.: Condens. Matter **3**, 3353 (1991).
- [34] E. Fradkin and S. A. Kivelson, *Ineluctable complexity*, Nat. Phys. **8**, 864 (2012).
- [35] J. C. S. Davis and D.-H. Lee, *Concepts relating magnetic interactions, intertwined electronic orders, and strongly correlated superconductivity*, Proc. Natl. Acad. Sci. U.S.A. **110**, 17623 (2013).
- [36] S. Onari and H. Kontani, *Self-consistent Vertex Correction Analysis for Iron-based Superconductors: Mechanism of Coulomb Interaction-Driven Orbital Fluctuations*, Phys. Rev. Lett. **109**, 137001 (2012).
- [37] M. Tsuchiizu, Y. Ohno, S. Onari, and H. Kontani, *Orbital Nematic Instability in the Two-Orbital Hubbard Model: Renormalization-Group + Constrained RPA Analysis*, Phys. Rev. Lett. **111**, 057003 (2013).
- [38] M. Tsuchiizu, K. Kawaguchi, Y. Yamakawa, and H. Kontani, *Multistage electronic nematic transitions in cuprate superconductors: A functional-renormalization-group analysis*, Phys. Rev. B **97**, 165131 (2018).
- [39] Y. Yamakawa and H. Kontani, *Spin-Fluctuation-Driven Nematic Charge-Density Wave in Cuprate Superconductors: Impact of Aslamazov-Larkin Vertex Corrections*, Phys. Rev. Lett. **114**, 257001 (2015).
- [40] Y. Yamakawa, S. Onari, and H. Kontani, *Nematicity and Magnetism in FeSe and Other Families of Fe-Based Superconductors*, Phys. Rev. X **6**, 021032 (2016).
- [41] S. Onari, Y. Yamakawa, and H. Kontani, *Sign-Reversing Orbital Polarization in the Nematic Phase of FeSe due to the C_2 Symmetry Breaking in the Self-Energy*, Phys. Rev. Lett. **116**, 227001 (2016).
- [42] A. V. Chubukov, M. Khodas, and R. M. Fernandes, *Magnetism, Superconductivity, and Spontaneous Orbital Order in Iron-Based Superconductors: Which Comes First and Why?*, Phys. Rev. X **6**, 041045 (2016).
- [43] R. M. Fernandes, P. P. Orth, and J. Schmalian, *Intertwined Vestigial Order in Quantum Materials: Nematicity and Beyond*, Annu. Rev. Condens. Matter Phys. **10**, 133 (2019).
- [44] S. Onari and H. Kontani, *$SU(4)$ Valley+Spin Fluctuation Interference Mechanism for Nematic Order in Magic-Angle Twisted Bilayer Graphene: The Impact of Vertex Corrections*, Phys. Rev. Lett. **128**, 066401 (2022).
- [45] H. Kontani, R. Tazai, Y. Yamakawa, and S. Onari, *Unconventional density waves and superconductivities in Fe-based superconductors and other strongly correlated electron systems*, Adv. Phys. **70**, 355 (2021).
- [46] S. Zhou and Z. Wang, *Chern Fermi pocket, topological pair density wave, and charge-4e and charge-6e superconductivity in kagome superconductors*, Nat. Commun. **13**, 7288 (2022).

- [47] Y.-M. Wu, R. Thomale, S. Raghu, *Sublattice Interference promotes Pair Density Wave order in Kagome Metals*, Phys. Rev. B **108**, L081117 (2023).
- [48] Z. Pan, C. Lu, F. Yang, C. Wu, *Frustrated superconductivity and charge-6e ordering*, arXiv:2209.13745 (available at <https://arxiv.org/abs/2209.13745>).
- [49] Q. Chen, D. Chen, W. Schnelle, C. Felser, and B. D. Gaulin, *Charge Density Wave Order and Fluctuations above T_{CDW} and below Superconducting T_c in the Kagome Metal CsV_3Sb_5* , Phys. Rev. Lett. **129**, 056401 (2022).
- [50] K. Yang, W. Xia, X. Mi, L. Zhang, Y. Gan, A. Wang, Y. Chai, X. Zhou, X. Yang, Y. Guo, M. He, *Charge fluctuations above T_{CDW} revealed by glasslike thermal*, Phys. Rev. B **107**, 184506 (2023).
- [51] R. Tazai, S. Matsubara, Y. Yamakawa, S. Onari, and H. Kontani, *A Rigorous Formalism of Unconventional Symmetry Breaking in Fermi Liquid Theory and Its Application to Nematicity in $FeSe$* , Phys. Rev. B **107**, 035137 (2023).
- [52] H.-M. Guo and M. Franz, *Topological insulator on the kagome lattice*, Phys. Rev. B **80**, 113102 (2009).
- [53] Y. Hu, X. Wu, B. R. Ortiz, S. Ju, X. Han, J. Ma, N. C. Plumb, M. Radovic, R. Thomale, S. D. Wilson, A. P. Schnyder, and M. Shi, *Rich nature of Van Hove singularities in Kagome superconductor CsV_3Sb_5* , Nature **13**, 2220 (2022).
- [54] Y. Luo, S. Peng, S. M. L. Teicher, L. Huai, Y. Hu, B. R. Ortiz, Z. Wei, J. Shen, Z. Ou, B. Wang, Y. Miao, M. Guo, M. Shi, S. D. Wilson, and J.-F. He, *Distinct band reconstructions in kagome superconductor CsV_3Sb_5* , Phys. Rev. B **105**, L241111 (2022).
- [55] K. Nakayama, Y. Li, T. Kato, M. Liu, Z. Wang, T. Takahashi, Y. Yao, and T. Sato, *Multiple energy scales and anisotropic energy gap in the charge-density-wave phase of the kagome superconductor CsV_3Sb_5* , Phys. Rev. B **104**, L161112 (2021).
- [56] Z. Liu, N. Zhao, Q. Yin, C. Gong, Z. Tu, M. Li, W. Song, Z. Liu, D. Shen, Y. Huang, K. Liu, H. Lei, and S. Wang, *Charge-Density-Wave-Induced Bands Renormalization and Energy Gaps in a Kagome Superconductor RbV_3Sb_5* , Phys. Rev. X **11**, 041010 (2021).
- [57] Z. Wang, S. Ma, Y. Zhang, H. Yang, Z. Zhao, Y. Ou, Y. Zhu, S. Ni, Z. Lu, H. Chen, K. Jiang, L. Yu, Y. Zhang, X. Dong, J. Hu, H.-J. Gao, and Z. Zhao, *Distinctive momentum dependent charge-density-wave gap observed in CsV_3Sb_5 superconductor with topological Kagome lattice*, arXiv:2104.05556 (available at <https://arxiv.org/abs/2104.05556>).
- [58] R. Tazai, Y. Yamakawa, M. Tsuchiizu, and H. Kontani, *d- and p-wave Quantum Liquid Crystal Orders in Cuprate Superconductors, κ -(BEDT-TTF) $_2X$, and Coupled Chain Hubbard Models: Functional-renormalization-group Analysis*, J. Phys. Soc. Jpn. **90**, 111012 (2021).
- [59] H. Kontani and S. Onari, *Orbital-Fluctuation-Mediated Superconductivity in Iron Pnictides: Analysis of the Five-Orbital Hubbard-Holstein Model*, Phys. Rev. Lett. **104**, 157001 (2010).
- [60] H. Tan, Y. Liu, Z. Wang, and B. Yan, *Charge Density Waves and Electronic Properties of Superconducting Kagome Metals*, Phys. Rev. Lett. **127**, 046401 (2021).
- [61] H. Li, T. T. Zhang, T. Yilmaz, Y. Y. Pai, C. E. Marvinney, A. Said, Q. W. Yin, C. S. Gong, Z. J. Tu, E. Vescovo, C. S. Nelson, R. G. Moore, S. Murakami, H. C. Lei, H. N. Lee, B. J. Lawrie, and H. Miao, *Observation of Unconventional Charge Density Wave without Acoustic Phonon Anomaly in Kagome Superconductors AV_3Sb_5 ($A = Rb, Cs$)*, Phys. Rev. X **11**, 031050 (2021).
- [62] Z. X. Wang, Q. Wu, Q. W. Yin, C. S. Gong, Z. J. Tu, T. Lin, Q. M. Liu, L. Y. Shi, S. J. Zhang, D. Wu, H. C. Lei, T. Dong, and N. L. Wang, *Unconventional charge density wave and photoinduced lattice symmetry change in the kagome metal CsV_3Sb_5 probed by time-resolved spectroscopy*, Phys. Rev. B **104**, 165110 (2021).
- [63] T. Moriya and K. Ueda, *Spin fluctuations and high temperature superconductivity*, Adv. Phys. **49**, 555 (2000).
- [64] Y. Vilk, and A.-M.S. Tremblay, *Non-perturbative many-body approach to the Hubbard model and single-particle pseudogap*, J. Phys I (France) **7**, 1309 (1997).
- [65] H. Kontani, *Anomalous transport phenomena in Fermi liquids with strong magnetic fluctuations*, Rep. Prog. Phys. **71**, 026501 (2008).
- [66] R. Tazai, Y. Yamakawa, and H. Kontani, *Emergence of charge loop current in the geometrically frustrated Hubbard model: A functional renormalization group study*, Phys. Rev. B **103**, L161112 (2021).
- [67] H. Kino and H. Kontani, *Phase Diagram of Superconductivity on the Anisotropic Triangular Lattice Hubbard Model: An Effective Model of κ -(BEDT-TTF) Salts*, J. Phys. Soc. Jpn. **67**, 3691 (1998); M. Kitatani, N. Tsuji, and H. Aoki, *FLEX+DMFT approach to the d-wave superconducting phase diagram of the two-dimensional Hubbard model*, Phys. Rev. B **92**, 085104 (2015).
- [68] Y. Xing, S. Bae, E. Ritz, F. Yang, T. Birol, A. N. C. Salinas, B. R. Ortiz, S. D. Wilson, Z. Wang, R. M. Fernandes, and V. Madhavan, *Optical Manipulation of the Charge Density Wave state in RbV_3Sb_5* , arXiv:2308.04128 (available at <https://arxiv.org/abs/2308.04128>).
- [69] X. Feng, K. Jiang, Z. Wang, and J. Hu, *Chiral flux phase in the Kagome superconductor AV_3Sb_5* , Sci. Bull. **66**, 1384 (2021).
- [70] H. Kontani, T. Tanaka, D. S. Hirashima, K. Yamada, and J. Inoue, *Giant Orbital Hall Effect in Transition Metals: Origin of Large Spin and Anomalous Hall Effects*, Phys. Rev. Lett. **102**, 016601 (2009).
- [71] H. Kontani, T. Tanaka, and K. Yamada, *Intrinsic anomalous Hall effect in ferromagnetic metals studied by the multi-d-orbital tight-binding model*, Phys. Rev. B **75**, 184416 (2007).
- [72] N. Nagaosa, J. Sinova, S. Onoda, A. H. MacDonald, and N. P. Ong, *Anomalous Hall effect*, Rev. Mod. Phys. **82**, 1539 (2010).
- [73] R. Nandkishore, L. S. Levitov, A. V. Chubukov, *Chiral superconductivity from repulsive interactions in doped graphene*, Nat. Phys. **8**, 158 (2012).
- [74] H. D. Scammell, J. Ingham, T. Li, and O. P. Sushkov, *Chiral excitonic order from twofold van Hove singularities in kagome metals*, Nat. Commun. **14**, 605 (2023).
- [75] C. Guo, G. Wagner, C. Putzke, D. Chen, K. Wang, L. Zhang, M. G. Amigo, I. Errea, M. G. Vergniory, C. Felser, M. H. Fischer, T. Neupert, and P. J. W. Moll, *Correlated order at the tipping point in the kagome metal CsV_3Sb_5* , arXiv:2304.00972 (available at <https://arxiv.org/abs/2304.00972>).
- [76] R. Tazai, Y. Yamakawa and H. Kontani, *Drastic magnetic-field-induced chiral current order and emergent current-bond-field interplay in kagome metal AV_3Sb_5 ($A=Cs,Rb,K$)*, arXiv:2303.00623 (available at

- <https://arxiv.org/abs/2303.00623>).
- [77] H. W. S. Arachchige, W. R. Meier, M. Marshall, T. Mat-suoka, R. Xue, M. A. McGuire, R. P. Hermann, H. Cao, and D. Mandrus, *Charge Density Wave in Kagome Lat-tice Intermetallic ScV_6Sn_6* , Phys. Rev. Lett. **129**, 216402 (2022).
 - [78] H. Hu, Y. Jiang, D. Calug, X. Feng, D. Subires, M. G. Vergniory, C. Felser, S. Blanco-Canosa, and B. A. Bernevig, *Kagome Materials I: SG 191, ScV_6Sn_6 . Flat Phonon Soft Modes and Un-conventional CDW Formation: Microscopic and Effective Theory*, arXiv:2305.15469 (available at <https://arxiv.org/abs/2305.15469>).
 - [79] A. Korshunov, H. Hu, D. Subires, Y. Jiang, D. Calugaru, X. Feng, A. Rajapitamahuni, C. Yi, S. Roychowdhury, M. G. Vergniory, J. Strempfer, C. Shekhar, E. Vescovo, D. Chernyshov, A. H. Said, A. Bosak, C. Felser, B. Andrei Bernevig, S. Blanco-Canosa, *Softening of a flat phonon mode in the kagome ScV_6Sn_6* , arXiv:2304.09173 (avail-able at <https://arxiv.org/abs/2304.09173>).
 - [80] Z. Guguchia, D.J. Gawryluk, Soohyeon Shin, Z. Hao, C. Mielke III, D. Das, I. Plokhikh, L. Liborio, K. Shenton, Y. Hu, V. Sazgari, M. Medarde, H. Deng, Y. Cai, C. Chen, Y. Jiang, A. Amato, M. Shi, M.Z. Hasan, J.-X. Yin, R. Khasanov, E. Pomjakushina, and H. Luetkens, *Hidden magnetism uncovered in charge ordered bilayer kagome material ScV_6Sn_6* , arXiv:2304.06436 (available at <https://arxiv.org/abs/2304.06436>).
 - [81] F. Grandi, A. Consiglio, M. A. Sentef, R. Thomale, and D. M. Kennes, *Theory of nematic charge orders in kagome metals*, Phys. Rev. B **107**, 155131 (2023)
 - [82] H. Yang, Y. Ye, Z. Zhao, J. Liu, X.-W. Yi, Y. Zhang, J. Shi, J.-Y. You, Z. Huang, B. Wang, J. Wang, H. Guo, X. Lin, C. Shen, W. Zhou, H. Chen, X. Dong, G. Su, Z. Wang, H.-J. Gao, *Superconductivity and orbital-selective nematic order in a new titanium-based kagome metal $CsTi_3Bi_5$* , arXiv:2211.12264 (available at <https://arxiv.org/abs/2211.12264>).
 - [83] H. Li, S. Cheng, B. R. Ortiz, H. Tan, D. Werhahn, K. Zeng, D. Jorhendt, B. Yan, Z. Wang, S. D. Wilson, and I. Zeljkovic, *Electronic nematicity in the absence of charge density waves in a new titanium-based kagome metal*, Nat. Phys. (2023). <https://doi.org/10.1038/s41567-023-02176-3>
 - [84] J. Huang, Y. Yamakawa, R. Tazai, and H. Kontani, *Odd-parity intra-unit-cell bond-order and induced ne-maticity in kagome metal $CsTi_3Bi_5$ driven by quantum interference mechanism*, arXiv:2305.18093 (available at <https://arxiv.org/abs/2305.18093>).

[Supplementary Information]

Charge-loop current order and Z_3 -nematicity mediated by bond order fluctuations in kagome metals

Rina Tazai¹, Youichi Yamakawa², and Hiroshi Kontani²

¹Yukawa Institute for Theoretical Physics, Kyoto University, Kyoto 606-8502, Japan

²Department of Physics, Nagoya University, Furo-cho, Nagoya 464-8602, Japan.

Supplementary Note 1: Square-lattice kagome model

In this Supplementary Information, we set the hopping integrals $t = -0.5$ eV and $t' = 0$. Hereafter, the unit of energy is eV unless otherwise noted. In Ref. [1], the present authors found that the paramagnon-interference theory naturally explains the bond order (BO) on the basis of the kagome-lattice Hubbard model. The used lattice structure with the square unit cell and its Fermi surface (FS) are shown in Supplementary Figs. 1 **a** and **b**, respectively. The van-Hove singular point at $\mathbf{k} = \mathbf{k}_X$ ($X=A,B,C$) is composed of the X -sublattice. The form factor of the $3Q$ BO and that of the $3Q$ cLC in real space are shown in Supplementary Figs. 1 **c** and **d**, respectively. We stress that the D_{6h} point group symmetry of the original kagome lattice is not harmed in the present DW equation solution using this square-lattice model.

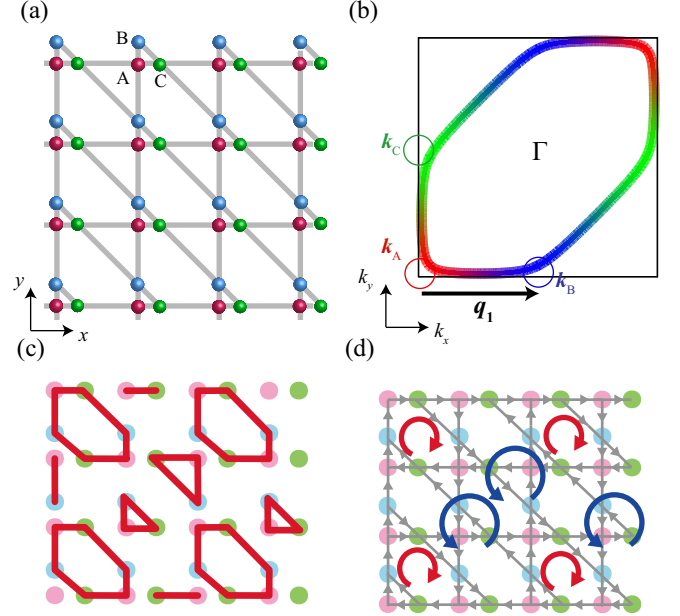
Supplementary Note 2: BO fluctuations due to Fock term by V

Here, we discuss the important effect of the nearest-site Coulomb interaction V in addition to the on-site one U .

Supplementary Note 2-1: HF approximation for the U - V Hubbard model

The analysis of the kagome-lattice U - V Hubbard model based on the mean-field theory is presented in Section SF of Ref. [1]. The charge (spin) channel eigenvalue $\lambda^{c(s)}$ in the mean-field theory is given by solving the linearized DW equation with the Hartree-Fock (HF) kernel function made of U and V . Its diagrammatic expression for V is shown in Supplementary Fig. 2 **a**.

Supplementary Figure 2 **b** shows the obtained several largest eigenvalues, λ_{SDW}^s and λ_X^c ($X=\text{CDW, BO, cLC}$), as functions of V/U at $U = 0.79$ [1]. These eigenvalues linearly increase with respect to U and V at a fixed V/U . When $V/U \ll 1$, a simple SDW order ($f = 1$) at $\mathbf{q} \approx \mathbf{0}$ is realized for $U \sim 1.6$. It originates from the Hartree term of U . When $V/U \gg 1$, on the other hand, simple charge-density-wave (CDW) order ($f = 1$) at $\mathbf{q} \approx \mathbf{q}_n$ is caused



Supplementary Fig. 1: **a**. Square-lattice kagome metal model that is convenient for the numerical study. **b**. Obtained Fermi surface (FS) in the square Brillouin zone. The color represents the weight of the sublattice ($A = \text{red}$, $B = \text{blue}$, $C = \text{green}$). **c**. Form factor of the $3Q$ bond order (BO) in real space. The red bonds represent the Tri-Hexagonal pattern. **d**. Form factor of the $3Q$ charge loop current (cLC). The coexistence of **c** and **d** leads to the C_6 symmetry state.

by the Hartree term of V . In this model, $\mathbf{q}_1 = (\pi, 0)$, $\mathbf{q}_2 = (\pi, \pi)$, $\mathbf{q}_3 = (0, \pi)$. For $V/U = 0.4 \sim 0.65$, the BO is realized by the Fock term of V . Note that the non-local BO is not suppressed by U , while the simple CDW order due to the Hartree term of V is strongly suppressed by U . However, the cLC instability is smaller than other instabilities within the HF approximation.

The form factors of the BO between the nearest sites in the square kagome-lattice model in Supplementary Fig. 1 **a** are given by

$$b_{AB}(\mathbf{q}) = (1 - e^{-iq_y})/2, \quad (1)$$

$$b_{BC}(\mathbf{q}) = (1 - e^{-iq_x + iq_y})/2, \quad (2)$$

$$b_{CA}(\mathbf{q}) = (1 - e^{iq_x})/2, \quad (3)$$

which are normalized as $\max_{\mathbf{q}}\{b_{lm}(\mathbf{q})\} = 1$. Here,

$$b_{lm}(\mathbf{q}) = b_{ml}(\mathbf{q})^* \text{ and } b_{ll}(\mathbf{q}) = 0.$$

Supplementary Note 2-2: Effective interaction due to BO susceptibility

In Supplementary Fig. 2 **b**, we found the development of the BO instability within the mean-field approximation. Next, we derive the effective interaction mediated by the BO susceptibility. The final result is given in Supplementary Eq. (16), which is essentially equivalent to Eq. (10) derived in the main text.

From now on, we derive Supplementary Eq. (16). First, we consider the effective interaction due to the Fock term of V . The Hamiltonian is $H_V = \sum_{il,jm,\sigma\sigma'} V_{il,jm} c_{il,\sigma}^\dagger c_{jm,\sigma} c_{jm,\sigma'}^\dagger c_{il,\sigma'}$, where i, j represent the unit cell, $l, m = A, B, C$, and c_{il} is the electron annihilation operator. (Here, we drop the spin indices for simplicity.) H_V is rewritten as $H_V = \frac{1}{N} \sum_{\mathbf{k}\mathbf{k}'\mathbf{q}\sigma\sigma'} V_{lm}(\mathbf{q}) c_{\mathbf{k}+\mathbf{q},l,\sigma}^\dagger c_{\mathbf{k},l,\sigma} c_{\mathbf{k}',m,\sigma'}^\dagger c_{\mathbf{k}'+\mathbf{q},m,\sigma'}$. Here, $V_{lm}(\mathbf{q}) = \frac{1}{N} \sum_{i,j} V_{il,jm} e^{-i\mathbf{q}\cdot(\mathbf{r}_{i,l}-\mathbf{r}_{j,m})}$, where $\mathbf{r}_{i,l}$ is the coordinate of the site (i, l) ; In Supplementary Fig. 1 **a**, $\mathbf{r}_{i,l} = (i_x, i_y)$ is independent of l , and i_x, i_y are integer coordinates. In the case of the nearest-site Coulomb interaction V , $V_{lm}(\mathbf{q})$ is expressed as

$$V_{lm}(\mathbf{q}) = 2V a_{lm}(\mathbf{q}). \quad (4)$$

Here,

$$a_{AB}(\mathbf{q}) = (1 + e^{-iq_y})/2, \quad (5)$$

$$a_{BC}(\mathbf{q}) = (1 + e^{-iq_x + iq_y})/2, \quad (6)$$

$$a_{CA}(\mathbf{q}) = (1 + e^{iq_x})/2, \quad (7)$$

where $a_{lm}(\mathbf{q}) = a_{ml}(\mathbf{q})^*$ and $a_{ll}(\mathbf{q}) = 0$.

Considering the relation $a_{lm}(\mathbf{k} - \mathbf{k}') = a_{lm}(\mathbf{k})a_{lm}(\mathbf{k}')^* + b_{lm}(\mathbf{k})b_{lm}(\mathbf{k}')^*$, the Fock term $V_{lm}(\mathbf{k} - \mathbf{k}')$ in Supplementary Fig. 2 **c** is expressed as

$$\begin{aligned} V_{lm}(\mathbf{k} - \mathbf{k}') &= 2V [a_{lm}(\mathbf{k})a_{lm}(\mathbf{k}')^* + b_{lm}(\mathbf{k})b_{lm}(\mathbf{k}')^*] \\ &= 2V \sum_d^{a,b} d_{lm}(\mathbf{k})d_{lm}(\mathbf{k}')^* \end{aligned} \quad (8)$$

which is expressed in Supplementary Fig. 2 **c**. Note that $a_{AB}(\mathbf{k}) \approx a_{AB}(\mathbf{k}') \approx 0$ and $b_{AB}(\mathbf{k}) \approx b_{AB}(\mathbf{k}') \approx 1$ for $(l, m) = (A, B)$ and $(\mathbf{k}, \mathbf{k}') \approx (\mathbf{k}_A, \mathbf{k}_B)$. Because $a_{lm}(\mathbf{k})$ and $b_{lm}(\mathbf{k})$ are orthogonal, the form factor $g_{\mathbf{q}}^{lm}(\mathbf{k})$ for the largest eigenvalue of the DW equation is equal to $b_{lm}(\mathbf{k})$ within the Fock approximation.

We next consider the second-order term with respect to V shown in Supplementary Fig. 2 **c**:

$$\begin{aligned} V_{lm,l'm'}^{(2)}(\mathbf{k} - \mathbf{k}'; \mathbf{q}) &= \frac{T}{N} \sum_p V_{lm}(\mathbf{k} - \mathbf{p}) G_{ll'}(p + q) G_{m'm}(p) V_{l'm'}(\mathbf{p}) \\ &= (2V)^2 \sum_{d,d'}^{a,b} d_{lm}(\mathbf{k})(d_{l'm'}^*(\mathbf{k}'))^* \chi_{lm,l'm'}^{0dd'}(q), \end{aligned}$$

where $\chi_{lm,l'm'}^{0dd'}(q) = -\frac{T}{N} \sum_p (d_{lm}(\mathbf{p}))^* G_{ll'}(p + q) G_{m'm}(p) d_{l'm'}^*(\mathbf{p})$ ($d, d' = a, b$). In kagome metal model, $\chi_{lm,l'm'}^{0dd'}(q)$ takes large value only for $d = d'$ and $\mathbf{q} \sim \mathbf{q}_m$ ($m = 1, 2, 3$).

As we mentioned above, we obtain $a_{AB}(\mathbf{k}) \approx a_{AB}(\mathbf{k}') \approx 0$ and $b_{AB}(\mathbf{k}) \approx b_{AB}(\mathbf{k}') \approx 1$ for $(\mathbf{k}, \mathbf{k}') \approx (\mathbf{k}_A, \mathbf{k}_B)$. By considering these relations, we can drop a_{lm} in Supplementary Eqs. (8) and (9). Thus, the summation of the first and the second order terms is given as

$$2V b_{lm}(\mathbf{k}) b_{l'm'}(\mathbf{k}')^* [\hat{1} + 2V \hat{\chi}^{0b}(q)]_{lm,l'm'}, \quad (10)$$

where $\chi_{lm,l'm'}^{0b}(q) \equiv \chi_{lm,l'm'}^{0bb}(q)$.

Now, we consider all the ladder diagrams composed of the Fock terms shown in Supplementary Fig. 2 **d**. It is obtained as

$$W_{lm,l'm'}(k, k', q) \approx 2V b_{lm}(\mathbf{k}) b_{l'm'}(\mathbf{k}')^* [\hat{1} + 2V \hat{\chi}^b(q)]_{lm,l'm'} \quad (11)$$

which takes sizable value when $\mathbf{k} \approx \mathbf{k}_m$, $\mathbf{k}' \approx \mathbf{k}_{m'}$, and $\mathbf{q} \approx (\mathbf{k}_l - \mathbf{k}_m)$, $(\mathbf{k}_{l'} - \mathbf{k}_{m'})$ (modulo original reciprocal vectors). The BO susceptibility in Supplementary Eq. (11) is given by the solution of $\hat{\chi}^b(q) = \hat{\chi}^{0b}(q) + (2V) \hat{\chi}^{0b}(q) \hat{\chi}^b(q)$. It is expressed as

$$\hat{\chi}^b(q) = \hat{\chi}^{0b}(q) (\hat{1} - 2V \hat{\chi}^{0b}(q))^{-1}. \quad (12)$$

Thus, $\hat{W}(k, k', q)$ is proportional to the BO susceptibility $\hat{\chi}^b(q)$. (One can verify the relation $\hat{\chi}^b(q) = \hat{\chi}^{0b}(q) + \frac{T^2}{N^2} \sum_{kk'} \hat{A}(k, q) \hat{W}(k, k', q) \hat{A}(k', q)$, where $A_{ml,m'l'}(k, q) = G_{mm'}(k + q) G_{l'l}(k)$.)

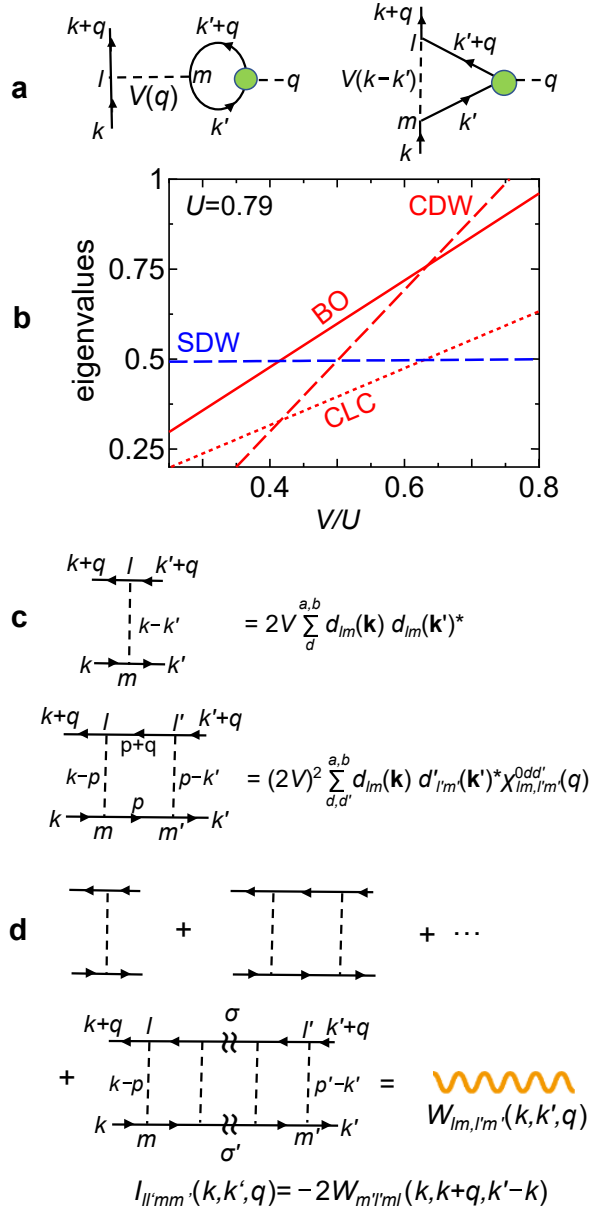
By using Supplementary Eq. (11), the charge-channel MT term in the DW equation is

$$I_{ll'mm'}(k, k', q) = -2W_{m'l'ml}(k, k + q, k' - k), \quad (13)$$

where the factor 2 comes from the summation of the parallel-spin (\uparrow, \uparrow) and the antiparallel-spin (\uparrow, \downarrow) ladder diagrams, because the Pauli principle does not work on V . It is expressed in Supplementary Fig. 2 **d**. Note that the present Fock term of the off-site Coulomb interaction corresponds to the Hartree term of the e -ph interaction in Eq. (2) in the main text.

As discussed above, $\chi_{lm,l'm'}^{0b}(q)$ is enlarged at $\mathbf{q} \approx \mathbf{q}_1$ only when $(lm, l'm') = (AB, AB), (AB, BA)$. (In the same way, it is enlarged at $\mathbf{q} \approx \mathbf{q}_2$ only when $(lm, l'm') = (BC, BC), (BC, CB)$.) For this reason, we can safely approximate Supplementary Eqs. (11) and (12) as the 2×2 matrix expressions for $\mathbf{q} \approx \mathbf{q}_n$ ($n = 1, 2, 3$).

Below, we explain that the relation $\chi_{AB,AB}^b(\mathbf{q}_1) \approx \chi_{AB,BA}^b(\mathbf{q}_1)$ holds. In kagome metals, the ratio in the irreducible susceptibility $\chi_{AB,BA}^{0b}(\mathbf{q}_1)/\chi_{AB,AB}^{0b}(\mathbf{q}_1)$ is just ~ 0.2 because the Green function $G_{lm}(k)$ is nearly diagonal ($\propto \delta_{l,m}$). Nonetheless of this fact, the ratio in the BO susceptibility $R \equiv \chi_{AB,BA}^b(\mathbf{q}_1)/\chi_{AB,AB}^b(\mathbf{q}_1)$ is of order unity, when the BO Stoner factor $\alpha_{BO} =$



Supplementary Fig. 2: **a**. Hartree and Fock terms with respect to the on-site (U) and the nearest-site (V) Coulomb interactions in the density-wave (DW) equation. Each green circle represents the form factor. **b**. Eigenvalues of the HF DW equation as a function of V/U : λ_{SDW}^s and λ_X^s ($X=\text{CDW}$, BO , CLC). Note that $\lambda_{\text{BO}}^s \approx \lambda_{\text{BO}}^s$; see Ref. [1]. **c**. The first and the second-order terms with respect to the Fock terms of V . **d** W given by the summation of all ladder-type diagrams, which is proportional to the BO susceptibility. The present Fock term corresponds to the Hartree term of the e -ph interaction in Eq. (2) in the main text.

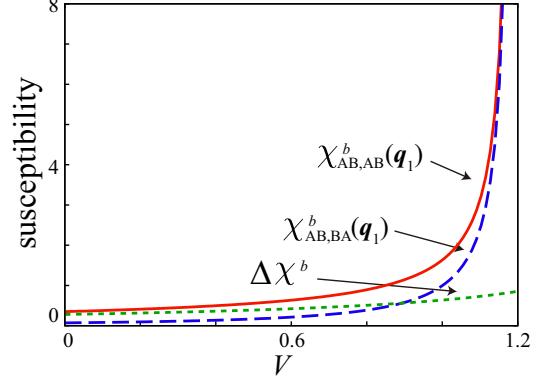
$2V(\chi_{\text{AB,AB}}^{0b}(\mathbf{q}_1) + \chi_{\text{AB,BA}}^{0b}(\mathbf{q}_1))$ is close to unity. In fact, for $\mathbf{q} \approx \mathbf{q}_1$, the relation between the BO susceptibility and its irreducible susceptibility is $\hat{\chi}^b = \hat{\chi}^{b0} + 2V\hat{\chi}^{b0}\hat{\chi}^b$, where $\hat{\chi}^{b0}$ is the 2×2 matrix: $\hat{\chi}^{b0} = \begin{pmatrix} \chi_{\text{AB,AB}}^{b0} & \chi_{\text{AB,BA}}^{b0} \\ \chi_{\text{BA,AB}}^{b0} & \chi_{\text{BA,BA}}^{b0} \end{pmatrix}$.

Then, the BO susceptibility for $\mathbf{q} \approx \mathbf{q}_1$ is obtained as

$$\chi_{\text{AB,AB}}^b(q) = [a - 2V(a^2 - b^2)]/d, \quad (14)$$

$$\chi_{\text{AB,BA}}^b(q) = b/d, \quad (15)$$

where $a \equiv \chi_{\text{AB,AB}}^{0b}(q)$, $b \equiv \chi_{\text{AB,BA}}^{0b}(q)$, and $d \equiv (1 - (a + b)2V)(1 - (a - b)2V)$.



Supplementary Fig. 3: $\chi_{\text{AB,AB}}^b$ and $\chi_{\text{AB,BA}}^b$ given in Supplementary Eqs. (14) and (15) as functions of V . We set $a = 0.35$ and $b/a = 0.2$. $\Delta\chi^b \equiv \chi_{\text{AB,AB}}^b - \chi_{\text{AB,BA}}^b$ is also shown.

According to Supplementary Eqs. (14) and (15), R becomes $b/a (\ll 1)$ when $V = 0$. In contrast, we obtain $R \approx 1$ at $\alpha_{\text{BO}} \approx 1$ ($\alpha_{\text{BO}} = (a + b)2V$). Supplementary Figure 3 shows the BO susceptibilities $\chi_{\text{AB,AB}}^b$ and $\chi_{\text{AB,BA}}^b$ as functions of V . We set $a = \chi_{\text{AB,AB}}^{b0}(\mathbf{q}_1) = 0.35$ and $b/a = 0.2$. Both $\chi_{\text{AB,AB}}^b$ and $\chi_{\text{AB,BA}}^b$ increase with V , while $\Delta\chi^b \equiv \chi_{\text{AB,AB}}^b - \chi_{\text{AB,BA}}^b$ is almost constant. This result means that the relation $R \approx 1$ holds near the BO-endpoint, around which the relation $\alpha_{\text{BO}} \lesssim 1$ holds.

According to Supplementary Eqs. (11) and (13), in the case of $R \approx 1$, the MT kernel function for the DW equation is simply given as

$$I_{ll',mm'}(k,k',q) \approx -g_{k'-k}^{m'l'}(k)g_{k-k'}^{lm}(k'+q) \times 2(2V)^2\chi^b(k-k'), \quad (16)$$

where $\chi^b(q) \equiv \chi_{\text{AB,AB}}^b(q) + \chi_{\text{AB,BA}}^b(q) \approx \chi_{\text{AB,AB}}^{b0}(q)/(1 - \alpha_{\text{BO}}(q))$ for $\mathbf{q} \approx \mathbf{q}_1$, and $g^{lm} \approx b_{lm}$ is the normalized BO form factor derived from the DW equation [1]. Supplementary Equation (16) is equal to Eq. (10) in the main text with $y = 2$. Note that both charge- and three spin-channel BO fluctuations develop in the present off-site V mechanism.

To summarize, the relation $\chi_{\text{AB,AB}}^b \approx \chi_{\text{AB,BA}}^b$ (*i.e.*, $R \approx 1$), which is assumed in the cLC mechanism in the main text, is well satisfied in the off-site V mechanism. Because this relation is also satisfied in the paramagnon-interference mechanism [1] and the phonon mechanism, these three different BO mechanisms will cooperate. We consider that the main mechanism of the BO in kagome

metals is the paramagnon interference mechanism [1], and both the bond-stretching phonon mode and the off-site Coulomb interaction will assist the BO formation.

Supplementary Note 2-3: The relation $y \gtrsim 1/2$ when v and V coexist

We consider the MT kernel function in the presence of both the off-site Coulomb interaction V and the BO interaction v in Eq. (2) in the main text. In this case, $y \gtrsim 1/2$ is expected to be realized. Considering the $SU(2)$ symmetry in spin space, the spin indices of the MT term in Supplementary Eq. (16) are written as [45]

$$I_{ll',mm'}^{\sigma\sigma',\rho\rho'}(k,k',q) = \frac{1}{2}I_{ll',mm'}^c(k,k',q)\delta_{\sigma,\sigma'}\delta_{\rho',\rho} + \frac{1}{2}I_{ll',mm'}^s(k,k',q)\boldsymbol{\sigma}_{\sigma,\sigma'} \cdot \boldsymbol{\sigma}_{\rho',\rho}, \quad (17)$$

where $\boldsymbol{\sigma}$ is the Pauli matrix vector. $\hat{I}^{s(c)}$ is the spin (charge) channel interaction given as $I_{ll',mm'}^{s(c)} = -g_{k'-k}^{m'l'}(k)g_{k-k'}^{lm}(k'+q)(2V)^2\chi^{b,s(c)}(k-k')$, where $\chi^{b,s(c)}(q) \approx \frac{\chi_{AB,AB}^{b0}(q)}{1-\alpha^{s(c)}(q)}$, and $\alpha^{s(c)}(q)$ is the spin (charge) channel Stoner factor. Based on Supplementary Eq. (17), the MT kernel function for the charge-channel form factor is given as $\hat{I}^{\text{MT}} = \frac{1}{2}(\hat{I}^c + 3\hat{I}^s)$ [45]. When $v = 0$, $\alpha_{s,c}(q)$ is equal to $\alpha_{\text{BO}}(q)$ and therefore $\hat{I}^c = \hat{I}^s$. As a result, $\hat{I}^{\text{MT}} = 2\hat{I}^c$ for $v = 0$, and therefore $y = 2$.

Here, we consider the effect of the BO interaction v . When $v > 0$, the charge Stoner factor is magnified as $\alpha_c(q) = \alpha_{\text{BO}}(q) + v\chi_g^0(\mathbf{q})$, where $\chi_g^0(\mathbf{q})$ is the irreducible susceptibility given by Eq. (5) in the main text. Thus, \hat{I}^c is enlarged by v . In contrast, the spin Stoner factor and \hat{I}^s are unchanged by v . Even if v is small but finite (e.g., $v\chi_g^0(\mathbf{q}) \sim 0.1$), the relation $\hat{I}^c \gg \hat{I}^s$ will be realized near the charge-channel BO criticality. Therefore, we obtain $\hat{I}^{\text{MT}} \approx \frac{1}{2}\hat{I}^c$, which means that $y \gtrsim 1/2$. To summarize, the relation $y \gtrsim 1/2$ is generally expected when V and v (= AL interference mechanism and e -ph interaction) coexist.

Supplementary Note 3: Self-consistent DW equation method: derivation of renormalized BO fluctuations

In the main text, we discuss the development of the BO susceptibility χ_g and its essential role in the cLC order. Based on the BO interaction model in Eq. (2) in the main text, we find that the MT term due to χ_g , $I^{\text{MT}} \sim -\chi_g$, leads to the emergence of the cLC order. On the other hand, I^{MT} also induces the renormalization of the χ_g itself. Here, we explain that the latter effect does not change the results of the main text. The kernel

function composed of the Hartree and MT terms, shown in Supplementary Fig. 4 a, are respectively given as

$$\tilde{I}_{\text{MT},\mathbf{q}}^{ll',mm'}(k,p) = -g_{\mathbf{p}-\mathbf{k}}^{m'l'}(\mathbf{k})g_{\mathbf{k}-\mathbf{p}}^{lm}(\mathbf{p}+\mathbf{q}) \times y\tilde{v}(1+\tilde{v}\tilde{\chi}_g(k-p)), \quad (18)$$

$$I_{\text{H},\mathbf{q}}^{ll',mm'}(k,p) = g_{\mathbf{q}}^{ll'}(k)v g_{\mathbf{q}}^{mm'}(p)^*, \quad (19)$$

where $\tilde{\chi}_g(q) = \chi_g^0(q)/(1-\tilde{v}\chi_g^0(q))$ is the renormalized BO susceptibility. In the main text, v in the DW equation for the cLC form factor and in the self-energy is considered as the renormalized \tilde{v} .

Here, by referring to the SCR theory [10], we perform the self-consistent calculation of the renormalized BO susceptibility, $\tilde{\chi}_g(q)$, based on the DW equation. A natural self-consistency condition for the MT term composed of BO susceptibility is

$$\lambda_{\mathbf{q}_1} = \tilde{\alpha}_{\text{BO}}, \quad (20)$$

where the left-hand side is the eigenvalue of the BO type form factor, and $\tilde{\alpha}_{\text{BO}} \equiv \tilde{v}\chi_g^0(\mathbf{q}_1)$ is the renormalized BO Stoner factor. Then, we can calculate the DW equation under the self-consistent condition of BO fluctuations. \tilde{v} given by Supplementary Eq. (20) is expressed as

$$\tilde{v} = v + v', \quad (21)$$

$$v' = \frac{T^2 \sum_{k,p,L,M} A_{g'}^L(k+\mathbf{q},-\mathbf{q}) I_{\text{MT},\mathbf{q}}^{L,M}(k,p) A_{g'}^M(p,\mathbf{q})}{(\chi_g^0(\mathbf{q}))^2}, \quad (22)$$

$$\hat{A}_{g'}(p,\mathbf{q}) = \hat{G}(p+\mathbf{q})\hat{g}'_{\mathbf{q}}(p)\hat{G}(p), \quad (23)$$

at $\mathbf{q} = \mathbf{q}_1$, where g' is the solution of the BO type form factor. The kernel function $I_{\mathbf{q}}(k,p)$ is shown in Supplementary Fig. 4 a. It is composed of the Hartree and MT terms. (Fock term is included in the MT term.) Because $g' \approx g$, \tilde{v} is simply derived from Supplementary Eq. (21) by setting $g' = g$. By using \tilde{v} , we solve the DW equation and show the obtained $\lambda_{\text{BO}} (= \tilde{\alpha}_{\text{BO}})$ and λ_{cLC} for $y = 1$ and $T = 0.01$ in Supplementary Fig. 4 b.

For small v ($\lesssim 0.2$), the DW equation solution in Supplementary Fig. 4 b corresponds to the HF approximation. When $f_{\mathbf{q}}(k)$ is BO form factor, the eigenvalue due to the Hartree term is equal to $\alpha_{\text{BO}} = 1.34v$. However, it is reduced to $\lambda_{\text{BO}} = 1.34(v+v')$, where $v' = -0.31yv$ is the Fock term contribution. When $f_{\mathbf{q}}(k)$ is the cLC form factor, the Hartree term vanishes, while the Fock term gives positive eigenvalue $\lambda_{\text{cLC}} = 1.34v''$ with $v'' = 0.26yv$. For large v ($\gtrsim 1$), the MT term becomes significant. For this reason, λ_{BO} saturates while λ_{cLC} strongly increases, and λ_{cLC} reaches unity at $v \approx 1.35$. This is because both $-v'$ and v'' are strongly enlarged by the MT term when $\tilde{\alpha}_{\text{BO}} \lesssim 1$.

Supplementary Figures 4 c and d show the obtained T_{cLC} and T_{BO} by solving the present DW equation, in the case of c $y = 1$ and d $y = 0.5$. Here, T_{cLC} is defined

by the condition $\lambda_{q_1} = 1$ for the cLC type form factor. Also, T_{BO} is defined as $\lambda_{q_1} = 0.985$ for the BO type form factor. The overall v -dependences of the order parameters are similar to those in Figs. 4 d and e in the main text. By introducing the self-energy, both T_{cLC} and T_{BO} will be suppressed, and the relation $T_{cLC} < T_{BO}$ will be realized in the strong coupling region.

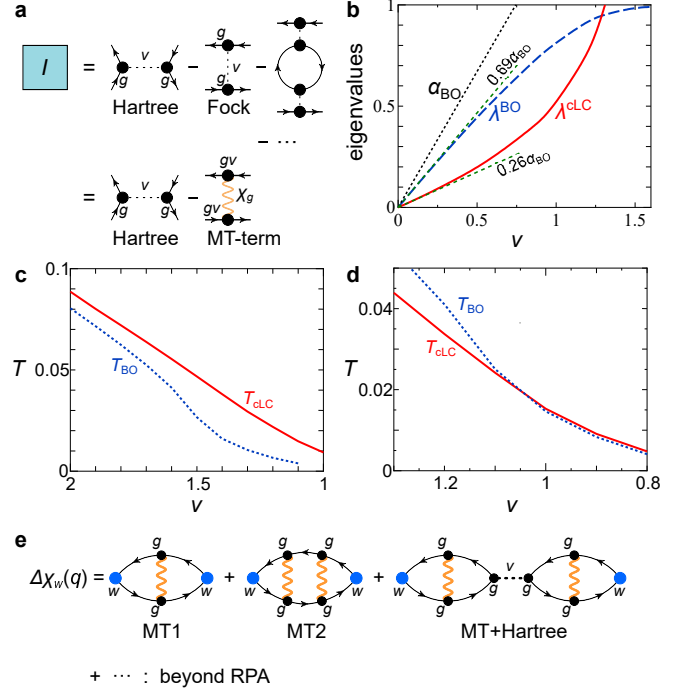
Supplementary Figure 4 e presents the beyond-RPA processes $\Delta\chi_w(q)$ in the present study. The total susceptibility is $\chi_w^{\text{tot}}(q) = \chi_w^{\text{RPA}}(q) + \Delta\chi_w(q)$. All these diagrams are generated by solving the DW equation. For $w = g$ (=BO form factor), $\chi_g^{\text{RPA}}(q)$ is large and positive, while $\Delta\chi_g(q)$ takes negative values due to the MT terms. For $w = f$ (=cLC form factor), $\chi_f^{\text{RPA}}(q)$ is very small, while $\Delta\chi_f(q)$ takes positive values, which becomes significant when $\alpha_{BO} \sim 1$. Therefore, the cLC susceptibility $\chi_f^{\text{tot}}(q)$ develops as large as the BO susceptibility in the present theory.

In the main text, we solve the DW equation with including the self-energy, while we solve the DW equation under the self-consistent condition in Supplementary Eq. (20) in this section. We find that two different DW equation analyses with MT-type kernel function produce essentially equivalent numerical results. The present self-consistent DW equation analysis strongly supports the reliability of the numerical study in the main text.

Supplementary Note 4: Effects of AL-type VCs

Here, we examine the role of the Aslamazov-Larkin (AL) vertex corrections (VCs) due to the interference between two bosonic susceptibilities (χ^{boson}) shown in Supplementary Fig. 5. The AL terms are significant for the even-parity order parameter in the paramagnon-interference mechanism. This mechanism is responsible for the BO and the orbital order in Fe-based superconductors [2, 3, 9], high- T_c cuprates [5, 6, 11], and kagome metals [1]. In contrast, the AL term is unimportant for the odd-parity order parameter, and instead, the MT term is significant for the current order in the frustrated Hubbard models [7] and non-Fermi liquid transport phenomena [8].

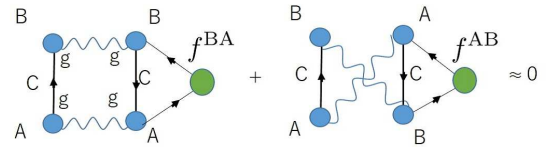
Here, we explain that the AL terms due to the bond susceptibilities, which were neglected in the main text, are unimportant in the present cLC mechanism in kagome metals. Supplementary Figure 5 exhibits the VC for $f_{q_1}^{\text{AB}}(\mathbf{k})$ at $\mathbf{k} \approx \mathbf{k}_A$. These terms are almost canceled for the odd-parity cLC order because of the relation $f_{q_1}^{\text{AB}}(\mathbf{k}) = -f_{q_1}^{\text{BA}}(-\mathbf{k} - \mathbf{q})$. In fact, the order parameter in the real space satisfies the relation $\delta t_{ij} = \mathcal{P}\delta t_{ji}$, where $\mathcal{P} = +1$ (-1) for the even (odd) parity order and $l, m = A, B, C$. Then, its Fourier transform gives the



Supplementary Fig. 4: **a.** Diagrammatic expression of the kernel function. **b.** λ_{BO} , λ_{cLC} , and α_{BO} given by the present self-consistent density-wave (DW) equation method, for $y = 1$ and $T = 0.01$. **c.,d.** Obtained T_{cLC} and T_{BO} as functions of v derived from the self-consistent DW equation method, in the cases of **c** $y = 1.0$ and **d** $y = 0.5$. The self-energy correction is dropped in this calculation. **e.** Beyond-RPA processes $\Delta\chi_w(q)$ generated by solving the DW equation.

form factor:

$$\begin{aligned}
 f_{\mathbf{q}}^{lm}(\mathbf{k}) &= \frac{1}{N} \sum_i^{\text{sub-l}} \sum_j^{\text{sub-m}} \delta t_{ij} e^{-\mathbf{k} \cdot (\mathbf{r}_i - \mathbf{r}_j)} e^{-\mathbf{q} \cdot \mathbf{r}_j} \\
 &= \frac{1}{N} \sum_i^{\text{sub-l}} \sum_j^{\text{sub-m}} (\mathcal{P} \delta t_{ji}) e^{-\mathbf{k} \cdot (\mathbf{r}_i - \mathbf{r}_j)} e^{-\mathbf{q} \cdot \mathbf{r}_j} \\
 &= \mathcal{P} f_{\mathbf{q}}^{ml}(-\mathbf{k} - \mathbf{q}).
 \end{aligned} \tag{24}$$



Supplementary Fig. 5: Two Aslamazov-Larkin (AL) terms for the charge loop current (cLC) order at $\mathbf{q} = \mathbf{q}_1$. These terms are almost canceled for the cLC order with $f_{q_1}^{\text{AB}}(\mathbf{k}) = -f_{q_1}^{\text{BA}}(-\mathbf{k} - \mathbf{q}_1)$.

In addition, it is verified that each AL term in Supplementary Fig. 5 is small because the momentum summation is restricted by four g 's. (Note that $|g_{\mathbf{q}}^{lm}(\mathbf{k})| \leq 1$.)

Supplementary Note 5: Parquet RG theory for kagome metals: Derivation of cLC and BO instabilities

In the main text, we revealed the BO fluctuation-mediated cLC mechanism in kagome metals based on the DW equation method. The BO fluctuations in the MT term of the DW equation causes the scattering between three van-Hove singularity (vHS) points. It is found that the cLC and BO fluctuations develop cooperatively, as demonstrated in Figs. 4 c-f in the main text and Supplementary Fig. 4 b-d.

The aim of this section is to verify the idea of the BO fluctuation-mediated cLC based on a different reliable theoretical framework. Here, we study the kagome lattice model based on the parquet renormalization group (RG) formulation [13, 14]. Supplementary Figure 6 a represents the four scattering processes between three vHS points. g_1 is the backward scattering, g_3 is the Umklapp scattering, and g_2 and g_4 are the forward scatterings. A great merit of the RG method is that both particle-particle and particle-hole channels are treated on the same footing, while the details of the shape of the FS are dropped. Using g_i 's, Γ_{um} and Γ_{back} included in the kernel of the DW equation, which are introduced in the main text, are expressed in Supplementary Fig. 6 b. The BO (cLC) instability is given by $\Gamma_{\text{back}} + (-)\Gamma_{\text{um}}$.

Here, we solve the following parquet RG equation for the three vHS points model to obtain the renormalized g_i ($i = 1 \sim 4$) due to the electron correlation [13, 14]:

$$\frac{g_1}{dz} = 2dg_1(g_2 - g_1), \quad (25)$$

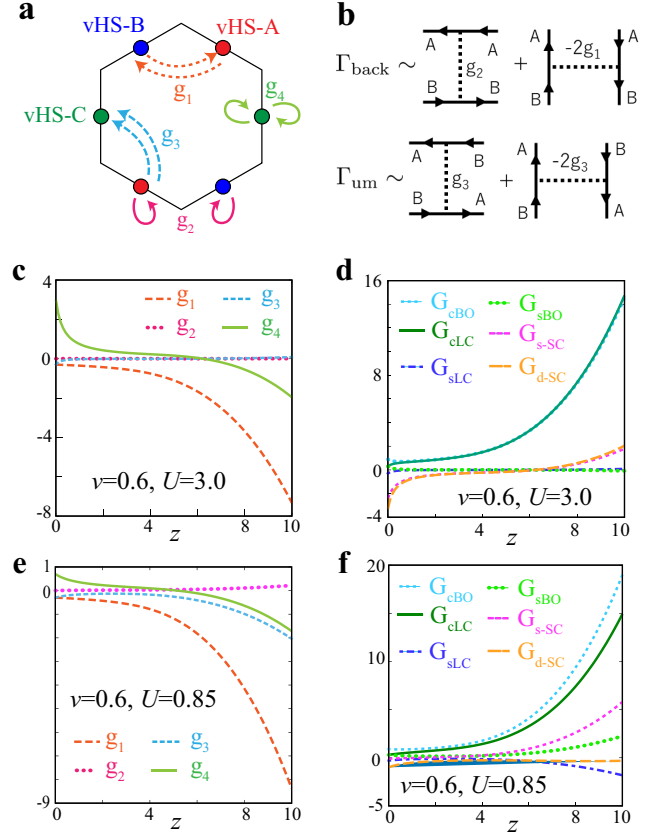
$$\frac{g_2}{dz} = 2d(g_2^2 + g_3^2), \quad (26)$$

$$\frac{g_3}{dz} = -g_3^2 - 2g_3g_4 + 2dg_3(2g_2 - g_1), \quad (27)$$

$$\frac{g_4}{dz} = -2g_3^2 - g_4^2, \quad (28)$$

where $z = \Pi^{0,AAAA}(\mathbf{0}, E) \sim \ln^2(E_0/E)$ and $d = d\chi^{0,ABBA}(\mathbf{q}_1, E)/dz$. Here, $\Pi^{0,AAAA}(\mathbf{0}, E)$ is the Cooper channel bubble with the low-energy (high-energy) cutoff E (E_0), and we consider the effect of the vHS at E_F . Note that E corresponds to $\sim T$, so $T \approx E_0 \exp(-z^{1/2})$. When $E_0 = 0.2\text{eV}$, $z = 10$ corresponds to $T \approx 100\text{K}$. The parameter d is bounded $0 < d < 1/2$, and $d = 1/2$ corresponds to the perfect nesting. Hereafter, we set $d = 1/4$ because the nesting of the real FS is not perfect. In this study, strong cLC and BO instabilities are robustly obtained for $d = 1/4 \sim 1/2$.

The BO interaction in Eq. (2) in the main text gives the following initial values at $z = 0$ (*i.e.*, $E = E_0$): $g_1^0 = g_3^0 = -v/2$, $g_2^0 = 0$. They correspond to $y = 1/2$ in the main text. Similar sets of $\{g_i^0\}$ were discussed in Ref. [13]. In addition, we include the on-site Coulomb interaction $g_4 = U$. Supplementary Figure 6 c shows the obtained flows of g_i 's as functions of z (≥ 0) for $v = 0.6$



Supplementary Fig. 6: **a.** Scattering processes between three vHS points; g_i ($i = 1 \sim 4$). **b.** Umklapp and backward terms in the kernel of the charge-channel density-wave (DW) equation. $\Gamma_{\text{um}} = -g_3$ and $\Gamma_{\text{back}} = g_2 - 2g_1$. $\Gamma_{\text{back}} + (-)\Gamma_{\text{um}}$ gives the cBO (cLC) instability. **c.** Obtained interactions $g_i(z)$ and **d.** instability for the channel X , G_X , ($X=\text{cBO}$, cLC, sBO, sLC, s-SC and d-SC) as function of y , in the case of $v = 0.6$ and $U = 3$. In this case, strong increment of $G_{\text{cBO}} \approx G_{\text{cLC}}$ are obtained. **e.** Obtained $g_i(z)$ and **f.** G_X in the case of $v = 0.6$ and $U = 0.7$. In this case, the relations $G_{\text{cBO}} \gtrsim G_{\text{cLC}}$ and $G_{\text{cLC}} \sim 2.5G_{\text{s-SC}}$ are obtained.

and $U = 3$. In this case, the renormalized g_1 takes a large negative value, while other g_i 's approach zero. In this case, the interaction for the X -channel susceptibility, G_X , is shown in Supplementary Fig. 6 d. G_X is given as [13, 14] $G_{\text{cBO}} = -2g_1 + g_2 - g_3$, $G_{\text{cLC}} = -2g_1 + g_2 + g_3$, $G_{\text{sBO}} = g_2 + g_3$, $G_{\text{sLC}} = g_2 - g_3$, $G_{\text{s-SC}} = -2g_3 - g_4$, and $G_{\text{d-SC}} = g_3 - g_4$. Here, $X=\text{c(s)BO}$: charge (spin) bond order, $X=\text{c(s)LC}$: charge (spin) loop-current, $X=\text{s(d)-SC}$: $s(d)$ -wave SC. Thus, both G_{cBO} and G_{cLC} strongly develop. The relation $G_{\text{cBO}} \approx G_{\text{cLC}}$ is obtained because g_3 is irrelevant. Therefore, we find $T_{\text{cBC}} \approx T_{\text{cLC}}$.

Supplementary Figure 6 e shows the obtained flow of g_i for $v = 0.6$ and $U = 0.7$. In this case, both $|g_3|$ and $|g_1|$ are enlarged. ($|g_1| > |g_3|$ is satisfied.) The corresponding instability G_X is shown in Supplementary Fig. 6 f. Thus, both G_{cBO} and G_{cLC} are strongly enlarged, while the relation $G_{\text{cBO}} \gtrsim G_{\text{cLC}} \gtrsim G_{\text{s-SC}}$ is obtained. Therefore,

we find $T_{\text{cBO}} \gtrsim T_{\text{cLC}} \gtrsim T_{s\text{-SC}}$.

Note that the CDW instability for the onsite operator $n_{\text{A}} + sn_{\text{B}}$ ($s = \pm 1$) at $\mathbf{q} = \mathbf{q}_1$ is $G_{\text{CDW},s} = s(g_1 - 2g_2) - g_4$. Also, the SDW instability for the onsite operator $m_{\text{A}} + sm_{\text{B}}$ ($m_{\text{A}} = n_{\text{A}\uparrow} - n_{\text{A}\downarrow}$) at $\mathbf{q} = \mathbf{q}_1$ is $G_{\text{SDW},s} = sg_1 + g_4$. Both quantities are smaller than G_{cBO} and G_{cLC} after the renormalization, as verified in Supplementary Figs. 6 d and f.

To summarize, the strong cLC instability derived from the present RG study strongly indicates the validity of the BO fluctuation-mediated cLC mechanism in kagome metals. Considering the initial condition $G_{\text{cLC}}^0 = G_{\text{cBO}}^0/3 = v/2$, the strong cLC instability originates from the beyond-RPA effect. The comparing study between the diagrammatic method and the RG method will lead to further interesting discoveries. On the other hand, parquet RG method cannot derive quantitative results, such as the long-range components of the order parameters obtained from the DW equations.

Supplementary Note 6: Stability of the nematic BO+cLC state

Supplementary Note 6-1: Analytic discussion

In the main text, we explained that the coexistence of the 3Q BO and the 3Q cLC leads to one C_6 state and three nematic (C_2) states. Here, we discuss the stability of these four states based on the Ginzburg-Landau (GL) theory. It is found that the nematic states are expected to emerge when $T_{\text{BO}} > T_{\text{cLC}}$ by considering the third-order GL terms, which play essential roles in kagome metals.

Here, we assume that the BO form factor g^{lm} is composed of the nearest-neighbor components, as we did in the main text. Then, the BO form factors $g_{\mathbf{q}_1}^{\text{AB}}(\mathbf{k})$, $g_{\mathbf{q}_2}^{\text{BC}}$ and $g_{\mathbf{q}_3}^{\text{CA}}$ are given by Supplementary Eqs. (1)-(3), respectively. The relation $g_{\mathbf{q}}^{lm}(\mathbf{k}) = \{g_{\mathbf{q}}^{ml}(\mathbf{k})\}^*$ is satisfied. As for the cLC form factor f^{lm} , we use the solution of the DW equation obtained in the main text. The obtained f^{lm} contains long-range components as shown in Fig. 3 c in the main text. In fact, its \mathbf{k} -space expression in Supplementary Figs. 8 a and b is very different from Supplementary Eq. (1). In addition, the frequency dependence f^{lm} shown in Supplementary Fig. 8 c is very strong, by reflecting drastic frequency dependence of the MT term ($\propto -\chi_g(q)$). The BO [cLC] parameter at $\mathbf{q} = \mathbf{q}_1$ is $\phi_1 g_{\mathbf{q}}^{lm} [\eta_1 f_{\mathbf{q}}^{lm}]$ with $lm = \text{AB}$ or BA .

Here, we introduce the vector representation $\phi \equiv (\phi_1, \phi_2, \phi_3)$, and define $\phi_1 \equiv (\phi, \phi, \phi)/\sqrt{3}$ and $\phi_2 \equiv (-\phi, \phi, \phi)/\sqrt{3}$. When $\phi = \phi_1$, we obtain the Tri-Hexagonal (Star-of-David) pattern for $\phi > 0$ ($\phi < 0$) shown in Supplementary Fig. 1 c. (The free energy for ϕ is different from that for $-\phi$ due to the third-order term.) When $\phi = \phi_2$, we obtain the Tri-Hexagonal pattern for

$\phi < 0$, while it is displaced by \mathbf{a}_{AB} from Supplementary Fig. 1 c.

We also introduce the notation $\boldsymbol{\eta} \equiv (\eta_1, \eta_2, \eta_3)$, and define $\boldsymbol{\eta}_1 \equiv (\eta, \eta, \eta)/\sqrt{3}$ and $\boldsymbol{\eta}_2 \equiv (-\eta, \eta, \eta)/\sqrt{3}$. The cLC pattern in Supplementary Fig. 1 d is given by $\boldsymbol{\eta} = \boldsymbol{\eta}_1$ with $\eta > 0$, and the direction of the cLC is reversed when $\eta < 0$. (The free energy is unchanged by $\boldsymbol{\eta} \rightarrow -\boldsymbol{\eta}$.) When $\boldsymbol{\eta} = \boldsymbol{\eta}_2$, the cLC pattern is given by the parallel shift of Supplementary Fig. 1 d by \mathbf{a}_{AB} .

Hereafter, we construct the GL free energy up to the fourth-order terms:

$$F = F^{(2)} + F^{(3)} + F^{(4)}. \quad (29)$$

The second-order term is

$$F^{(2)} = a_1 |\phi|^2 + a_2 |\boldsymbol{\eta}|^2, \quad (30)$$

$$a_1 = -\chi_g^0(\mathbf{q}_1) + I_{\text{b}}^{-1}, \quad (31)$$

$$a_2 = -\chi_f^0(\mathbf{q}_1) + I_{\text{c}}^{-1}, \quad (32)$$

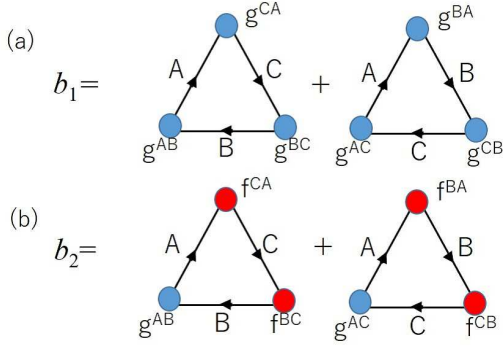
where $I_{\text{b(c)}} (> 0)$ is the effective interaction for the BO (cLC order) [11, 13]. ($a_{1,2} \leq 0$ corresponds to $\lambda_{\mathbf{q}} \geq 1$ in the DW equation as proved in Ref. [11].) Because $\chi_g^0(\mathbf{q}_1) \approx \chi_f^0(\mathbf{q}_1)$, the relation $T_{\text{BO}} > T_{\text{cLC}}$ would be realized when $I_{\text{b}} > I_{\text{c}}$. We note that, in the present theory, both I_{b} and I_{c} originate from the electron correlations, and therefore they exhibit strong T -dependences.

The third-order term and the forth-order term for general ϕ and $\boldsymbol{\eta}$ are given as

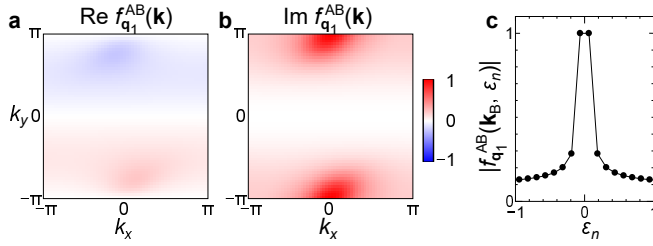
$$\begin{aligned} F^{(3)} &= b_1 \phi_1 \phi_2 \phi_3 + b_2 (\phi_1 \eta_2 \eta_3 + \eta_1 \phi_2 \eta_3 + \eta_1 \eta_2 \phi_3), \quad (33) \\ F^{(4)} &= d_{1,a} (\phi_1^4 + \phi_2^4 + \phi_3^4) + d_{1,b} (\phi_1^2 \phi_2^2 + \phi_2^2 \phi_3^2 + \phi_3^2 \phi_1^2) \\ &\quad + d_{2,a} (\eta_1^4 + \eta_2^4 + \eta_3^4) + d_{2,b} (\eta_1^2 \eta_2^2 + \eta_2^2 \eta_3^2 + \eta_3^2 \eta_1^2) \\ &\quad + 2d_{3,a} (\phi_1^2 \eta_1^2 + \phi_2^2 \eta_2^2 + \phi_3^2 \eta_3^2) \\ &\quad + d_{3,b} (\phi_1^2 \eta_2^2 + \phi_2^2 \eta_3^2 + \phi_3^2 \eta_1^2 + \phi_2^2 \eta_1^2 + \phi_3^2 \eta_2^2 + \phi_1^2 \eta_3^2). \quad (34) \end{aligned}$$

Note that the term $\sim \phi_1 \phi_2 \eta_1 \eta_2$ is absent. In the absence of the cLC order, the third-order free energy term is given by the first term of Supplementary Eq. (33). The diagrammatic expression for the coefficient b_1 is given in Supplementary Fig. 7 a, and its analytic expression is found in Refs. [12, 13]. When the BO and the cLC coexist, we obtain the additional cross-terms given by the second term of Supplementary Eq. (33). The diagrammatic expression for b_2 is given in Supplementary Fig. 7 b. The relation $b_1 = -b_2$ holds when the relation $f_{\mathbf{q}_2}^{\text{BC}}(\mathbf{k}_{\text{C}}) f_{\mathbf{q}_3}^{\text{CA}}(\mathbf{k}_{\text{A}}) = -g_{\mathbf{q}_2}^{\text{BC}}(\mathbf{k}_{\text{C}}) g_{\mathbf{q}_3}^{\text{CA}}(\mathbf{k}_{\text{A}})$ holds. Note that the minimum of the GL free energy does not diverge due to the positive fourth-order term.

Now, we set $\phi = \phi_1$ because the 3Q BO is stabilized by the third-order GL free energy ($\propto \phi_1 \phi_2 \phi_3$), and it is actually observed experimentally. When $\boldsymbol{\eta} = \boldsymbol{\eta}_{1[2]}$, the BO+cLC state is C_6 [C_2] symmetric as shown in Fig. 5 a [b] in the main text. Hereafter, we explain that the



Supplementary Fig. 7: Diagrams for the third-order Ginzburg-Landau terms b_1 and b_2 . The relation $b_1 = -b_2$ holds when $f_{\mathbf{q}}^{lm}(\mathbf{k}) = \pm ig_{\mathbf{q}}^{lm}(\mathbf{k})$.



Supplementary Fig. 8: **a.** Real part and **b.** imaginary part of the cLC form factor $f_{\mathbf{q}_1}^{AB}(\mathbf{k})$ in the square kagome-lattice model. $f_{\mathbf{q}_1}^{AB}(\mathbf{k})$ is very different from the nearest-neighbor BO form factor $-ig_{\mathbf{q}_1}^{AB}(\mathbf{k}) = \frac{1}{2} \sin k_y - i\frac{1}{2}(1 - \cos k_y)$, and its strong \mathbf{k} -dependence means the existence of large cLC order between distant sites. This means that the inner-product $|\frac{1}{N} \sum_{\mathbf{k}} [i f_{\mathbf{q}}^{AB}(\mathbf{k})]^* g_{\mathbf{q}}^{AB}(\mathbf{k})|$ is small, indicating that the cLC and the BO are nearly independent. **c.** ϵ_n -dependence of $|f_{\mathbf{q}_1}^{AB}(\mathbf{k}_B, \epsilon_n)|$, where $y = 1$, $v = 1.0$ and $T = 0.02$.

C_2 -symmetric BO+cLC state is realized due to $\boldsymbol{\eta} \neq \boldsymbol{\eta}_1$, based on both analytic and numerical studies.

Here, we discuss the possible $3Q$ BO+cLC states in the case of $T_{\text{BO}} > T_{\text{cLC}}$. When $\phi = \phi_1$, the third-order term is

$$F^{(3)'} = \frac{b_1}{3\sqrt{3}}\phi^3 + \frac{b_2}{2\sqrt{3}}\phi[(\eta_1 + \eta_2 + \eta_3)^2 - |\boldsymbol{\eta}|^2]. \quad (35)$$

Now, we minimize Supplementary Eq. (35) under the constraints $|\boldsymbol{\eta}| = \text{const.}$ and $|\phi| = \text{const.}$, where the 2nd order GL free energy is constant. In the case of $|\boldsymbol{\eta}| \gg |\phi|$ ($T_{\text{cLC}} \gg T_{\text{BO}}$), $b_2\phi$ becomes negative and $\boldsymbol{\eta} = \boldsymbol{\eta}_1$ to get the energy gain from the second term in Supplementary Eq. (35). (The first term is small and positive because of $b_1 b_2 < 0$.) Thus, the coexisting state has C_6 symmetry.

In the case of $|\boldsymbol{\eta}| \ll |\phi|$ ($T_{\text{cLC}} \ll T_{\text{BO}}$), $b_1\phi$ becomes negative to get the energy gain from the first term in Supplementary Eq. (35). Then, the second term is minimized when $\eta_1 + \eta_2 + \eta_3 = 0$ for a fixed $|\boldsymbol{\eta}|$. For example,

$\boldsymbol{\eta}' \propto (\eta, \eta, -2\eta)$ or $\boldsymbol{\eta}'' \propto (\eta, -\eta, 0)$. In both cases, the coexisting state has C_2 symmetry. The nematic BO+cLC state with ϕ_1 and $\boldsymbol{\eta}'$ is depicted in Fig. 5 c in the main text. Note that the total free energy is unchanged under $\eta_1 + \eta_2 + \eta_3 = 0$ within the 4th-order GL terms, while this degeneracy is lifted by the 6th-order GL terms. Thus, the Z_3 nematic BO+cLC state by $\boldsymbol{\eta}'$ or $\boldsymbol{\eta}''$ is expected to be realized for $T < T_{\text{cLC}} < T_{\text{BO}}$, as shown in a schematic phase diagram in Fig. 4 f in the main text.

Finally, we discuss the fourth-order GL term in Supplementary Eq. (34). The coefficients $d_{l,a}$ and $d_{l,b}$ ($l = 1, 2, 3$) are positive, and they are given by the closed Feynman diagrams made of four form factors and four G 's [13]. The relations $d_{1,a} = d_{2,a} = d_{3,a}$ and $d_{1,b} = d_{2,b} = d_{3,b}$ hold in the case of $f_{\mathbf{q}}^{lm}(\mathbf{k}) \approx \pm ig_{\mathbf{q}}^{lm}(\mathbf{k})$. For any $\phi = \phi_\alpha$ and $\boldsymbol{\eta} = \boldsymbol{\eta}_\beta$ ($\alpha, \beta = 1, 2$), the fourth-order GL term is expressed as

$$F^{(4)'} = d_1\phi^4 + d_2\eta^4 + 2d_3\phi^2\eta^2, \quad (36)$$

where the coefficients are $d_1 = (d_{1,a} + d_{1,b})/3$, $d_2 = (d_{2,a} + d_{2,b})/3$, and $d_3 = (d_{3,a} + d_{3,b})/3$. However, the relation $f_{\mathbf{q}}^{lm}(\mathbf{k}) \approx \pm ig_{\mathbf{q}}^{lm}(\mathbf{k})$ is not satisfied because the mechanisms of the cLC and the BO are different in the present theory. Therefore, all the coefficients b_l , $d_{m,a}$, $d_{m,b}$ depend on $l = 1, 2$ and $m = 1, 2, 3$. In the successive section, we discuss the stability of the nematic BO+cLC state based on the numerical study.

Supplementary Note 6-2: Numerical study

Here, we calculate the 3rd- and 4th-order GL coefficients based on the diagrammatic method. We normalize the form factors as $\max_{\mathbf{k}} |g_{\mathbf{q}_1}^{AB}(\mathbf{k})| = \max_{\mathbf{k}, l, m} |f_{\mathbf{q}_1}^{AB}(\mathbf{k})| = 1$ which is realized at $\mathbf{k} = \mathbf{k}_A$ in the present DW equation analysis. Then, the BO parameter $\phi_m g_{\mathbf{q}_m}(\mathbf{k})$ at $\mathbf{q} = \mathbf{q}_m$ ($m = 1 \sim 3$) gives the hybridization gap $\Delta_{\text{BO}} \sim |\phi|$ in the folded band at Γ point. [In the same way, $\Delta_{\text{cLC}} \sim |\boldsymbol{\eta}|$ for the cLC order $\eta_m f_{\mathbf{q}_m}(\mathbf{k})$.] Thus, the present normalization rule for g and f is physically reasonable and convenient. Note that the normalization rule does not influence the physical quantities, because the change of H_{int} due to $g \rightarrow r \cdot g$ is absorbed by $v \rightarrow v/r^2$.

The 3rd order GL parameters per unit cell are given as

$$b_1 = 3I_{123}^{ggg} + 3I_{132}^{ggg}, \quad (37)$$

$$b_2 = 3I_{123}^{gff} + 3I_{132}^{gff}, \quad (38)$$

where

$$I_{lmn}^{xyz} = -\frac{T}{3N} \sum_{k, \sigma} \text{Tr} \hat{x}_{q_l}(k + q_n + q_m) \hat{G}(k + q_n + q_m) \times \hat{y}_{q_m}(k + q_n) \hat{G}(k + q_n) \hat{z}_{q_n}(k) \hat{G}(k), \quad (39)$$

where x, y, z is f or g , and l, m, n is 1, 2, or 3. The relation $q_l + q_m + q_n = 0$ should be satisfied. Here, $\hat{G}(k)$

is the 3×3 matrix expression of the Green function with the self-energy given in the main text.

The 4th order GL parameters per unit cell are given as

$$d_{1,a} = I_{1111}^{gggg}, \quad (40)$$

$$d_{1,b} = 2I_{1212}^{gggg} + 4I_{1122}^{gggg}, \quad (41)$$

$$d_{2,a} = I_{1111}^{ffff}, \quad (42)$$

$$d_{2,b} = 2I_{1212}^{ffff} + 4I_{1122}^{ffff}, \quad (43)$$

$$d_{3,a} = \frac{1}{2}(2I_{1111}^{fgfg} + 4I_{1111}^{ffgg}), \quad (44)$$

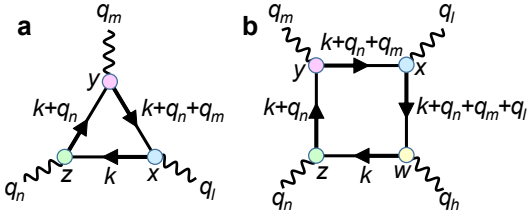
$$d_{3,b} = 2I_{1212}^{fgfg} + 4I_{1122}^{ffgg}, \quad (45)$$

where

$$\begin{aligned} I_{hlmn}^{wxyz} = & \frac{T}{4N} \sum_{k,\sigma} \text{Tr} \hat{w}_{q_h}(k + q_n + q_m + q_l) \hat{G}(k + q_n + q_m + q_l) \\ & \times \hat{x}_{q_l}(k + q_n + q_m) \hat{G}(k + q_n + q_m) \\ & \times \hat{y}_{q_m}(k + q_n) \hat{G}(k + q_n) \hat{z}_{q_n}(k) \hat{G}(k), \end{aligned} \quad (46)$$

where w, x, y, z is f or g , and h, l, m, n is 1, 2, or 3. The relation $q_h + q_l + q_m + q_n = 0$ should be satisfied. The diagrammatic expression of I_{lmn}^{xyz} and I_{hlmn}^{wxyz} are depicted in Supplementary Fig. 9.

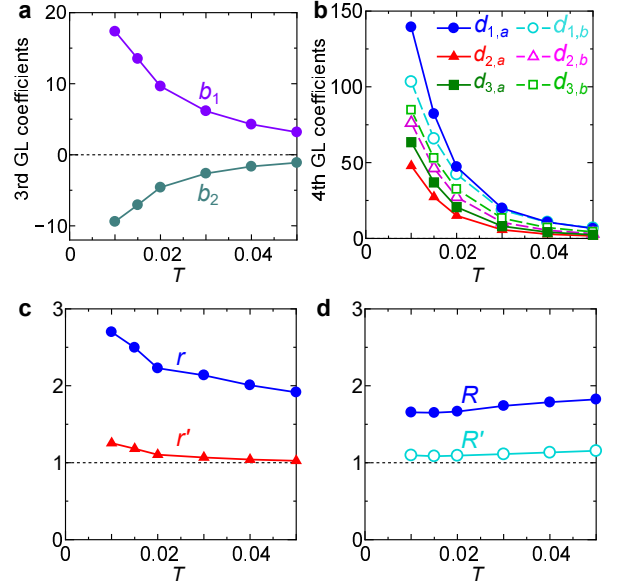
Note that these GL coefficients depend on the Green functions (=bandstructure) and the form factors g and f . Thus, the GL coefficients depend on the BO/cLC mechanisms indirectly, just through the form factors.



Supplementary Fig. 9: Diagrammatic expressions of Ginzburg-Landau parameters: **a**. Third-order term. **b**. Fourth-order term.

The numerical results of the 3rd and 4th GL parameters are shown in Supplementary Figs. 10 **a** and **b**, respectively, for $v = 0.6$ and $y = 1$. We find that b_1 and b_2 have different signs, consistently with the discussion in the previous section. The obtained GL coefficients exhibit moderate and monotonic T -dependences for a wide T range because the self-energy suppresses unrealistic singular behaviors of GL coefficients at low temperatures. As we show in Supplementary Fig. 10 **c**, the obtained ratio $r = 2d_{1,a}/d_{1,b}$ is larger than 1. This result means that experimentally observed 3Q BO state is realized irrespective of the size of b_1 . Also, the relation $r' = 2d_{2,a}/d_{2,b} > 1$ means that the 3Q cLC state is realized.

In addition, the obtained GL coefficients satisfy the relations $R = d_{1,a}d_{2,a}/d_{3,a}^2 > 1$ and $R' = d_{1,b}d_{2,b}/d_{3,b}^2 > 1$ as shown in Supplementary Fig. 10 **d**. These relations indicate the smallness of the competition between cLC and BO described by $d_{3,a}$ and $d_{3,b}$ terms. (Note that $R = R' = 1$ when the BO and cLC form factors are composed of only the nearest bonds [13].) Therefore, we can expect the coexistence of the BO and cLC orders by analyzing the GL free energy. The relations $R, R' > 1$ originates from the smallness of the inner-product $|\frac{1}{N} \sum_{\mathbf{k}} [i f_{\mathbf{q}}^{ml}(\mathbf{k})]^* g_{\mathbf{q}}^{lm}(\mathbf{k})|$ (see Supplementary Fig. 8 **a** and **b**) and the strong frequency dependence of the cLC form factor shown in Supplementary Fig. 8 **c**. This is not surprising because the driving forces of the BO and the cLC are different in the present theory.



Supplementary Fig. 10: **a,b**. Numerical results of the Ginzburg-Landau parameters for $v = 0.6$ as functions of T . The relation $b_1 b_2 < 0$ is verified. **c**. Ratio $r = 2d_{1,a}/d_{1,b}$ (for BO) and ratio $r' = 2d_{2,a}/d_{2,b}$ (for cLC). The 3Q state is stable when r (r') is larger than unity. **d**. Ratio $R = d_{1,a}d_{2,a}/d_{3,a}^2$ and ratio $R' = d_{1,b}d_{2,b}/d_{3,b}^2$. The C_2 symmetric BO+cLC coexisting state is energetically stable when $R, R' > 1$.

Supplementary Figure 11 **a** exhibits the obtained phase diagram derived from the GL free energy, by using the GL coefficients in Supplementary Figs. 10 **a** and **b** at $T = 0.01$. The horizontal (vertical) axis is the second-order GL parameter for the BO (a_1 (cLC a_2)). Each phase is determined by minimizing the GL free energy $F[\phi, \eta]$ with respect to the following 13^2 patterns $(\phi, \eta) = (\phi_m, \eta_n)$ with $m, n = 1 \sim 13$ exactly numerically:

$$\begin{aligned} 3Q \text{ BO : } & \phi_1 = \phi(1, 1, 1)/\sqrt{3}, \\ & \phi_2 = \phi(-1, 1, 1)/\sqrt{3}, \quad \phi_3, \phi_4 = \text{cycl.}, \\ 2Q \text{ BO : } & \phi_5 = \phi(1, 1, 0)/\sqrt{2}, \quad \phi_6, \phi_7 = \text{cycl.}, \\ & \phi_8 = \phi(1, -1, 0)/\sqrt{2}, \quad \phi_9, \phi_{10} = \text{cycl.}, \end{aligned}$$

1Q BO : $\phi_{11} = \phi(1, 0, 0)$, $\phi_{12}, \phi_{13} = \text{cycl.}$,

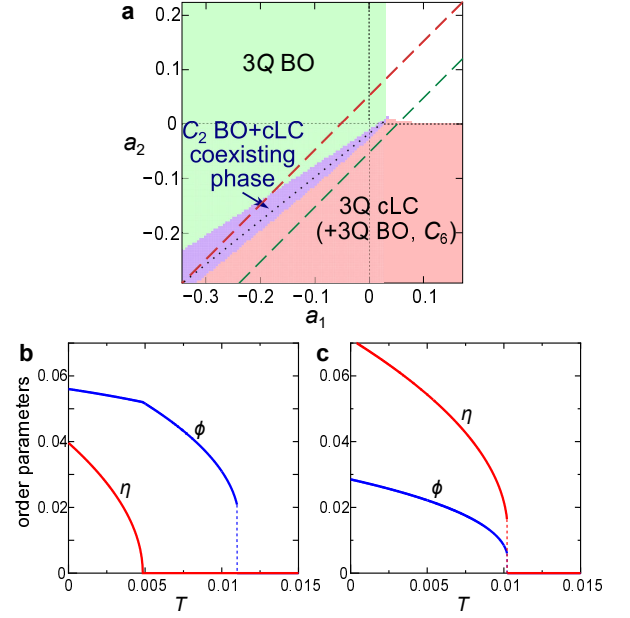
and $\eta_n = \phi_n|_{\phi \rightarrow \eta}$ for the cLC.

The obtained C_2 symmetric BO+cLC phase with $\phi = \phi_1$ and $\eta = (\eta, -\eta, 0)/\sqrt{2}$ (or equivalently $\eta = (\eta, \eta, -2\eta)/\sqrt{6}$; see E-1) is shown by the purple region. This C_2 coexisting phase is always realized when $T_{\text{BO}} \gtrsim T_{\text{cLC}}$. Also, the green (red) region corresponds to 3Q BO (cLC) phase. In the red region, the secondary 3Q BO appears through the b_2 -terms even for $a_1 > 0$, and $|\phi|$ becomes comparable to $|\eta|$ when $a_1 < 0$. The coexisting state is C_6 symmetry. [13].

In deriving the phase boundary between the C_2 and C_6 coexisting phases in Supplementary Fig. 11 a, we optimized three parameters $\{\phi, \phi', \eta\}$ numerically by considering additional 14th order parameter $\phi_{14} \sim (\phi, \phi, \phi')$ and $\eta \sim (\eta, -\eta, 0)$. The dotted line in Supplementary Fig. 11 a is the phase boundary by setting $\phi = \phi'$.

Supplementary Figure 11 b shows the obtained order parameters along the red broken line in a. Here, we set 2nd order GL parameters as functions of T : $a_1 = A_1(T/T_{\text{BO}}^0 - 1)$, $a_2 = A_2(T/T_{\text{cLC}}^0 - 1)$, where $A_1 = A_2 = 0.17$, $T_{\text{BO}}^0 = 0.01$ and $T_{\text{cLC}}^0 = 0.85T_{\text{BO}}^0$. Here, $A_{1(2)} = 0$ at $T = T_{\text{BO(cLC)}}^0$. The GL parameters at $T = 0.01$ in Supplementary Fig. 10 are used. We find that $|\phi|$ exhibits the 1st order transition at $T_{\text{BO}} \approx 1.1T_{\text{BO}}^0$, and $|\eta|$ appears as the 2nd-order transition at $T_{\text{cLC}} \approx 0.6T_{\text{cLC}}^0 \approx 0.5T_{\text{BO}}^0$. This result corresponds to the region $v > v^*$ in Fig. 4 f in the main text. By performing careful numerical analyses, we find that the C_2 coexisting region (=purple region in Supplementary Figure 11 a) appears when the relations $R > 1$ and $R' > 1$ are satisfied.

Supplementary Figure 11 c shows the order parameters along the green broken line in a. The primary 3Q cLC order induces the secondary 3Q BO due to the 3rd order GL terms. The symmetry of this coexisting phase is C_6 [13].



Supplementary Fig. 11: **a.** Obtained phase diagram using the Ginzburg-Landau coefficients in Supplementary Figs. 10 a and b at $T = 0.01$. The horizontal (vertical) axis is a_1 (a_2). The purple region represents the C_2 symmetric BO+cLC phase. The dotted line is the phase boundary without optimizing the C_2 BO and cLC order parameters. **b.,c.** Obtained order parameters along **b** the red broken line and **c** the green broken line in **a**.

-
- [1] R. Tazai, Y. Yamakawa, S. Onari, and H. Kontani, *Mechanism of exotic density-wave and beyond-Migdal unconventional superconductivity in kagome metal AV_3Sb_5 ($A = K, Rb, Cs$)*, Sci. Adv. **8**, eabl4108 (2022).
- [2] S. Onari and H. Kontani, *Self-consistent Vertex Correction Analysis for Iron-based Superconductors: Mechanism of Coulomb Interaction-Driven Orbital Fluctuations*, Phys. Rev. Lett. **109**, 137001 (2012).
- [3] Y. Yamakawa, S. Onari, and H. Kontani, *Nematicity and Magnetism in FeSe and Other Families of Fe-Based Superconductors*, Phys. Rev. X **6**, 021032 (2016).
- [4] S. Onari, Y. Yamakawa, and H. Kontani, *Sign-Reversing Orbital Polarization in the Nematic Phase of FeSe due to the C_2 Symmetry Breaking in the Self-Energy*, Phys. Rev. Lett. **116**, 227001 (2016).
- [5] M. Tsuchiizu, K. Kawaguchi, Y. Yamakawa, and H. Kontani, *Multistage electronic nematic transitions in cuprate superconductors: A functional-renormalization-group analysis*, Phys. Rev. B **97**, 165131 (2018).
- [6] Y. Yamakawa and H. Kontani, *Spin-Fluctuation-Driven Nematic Charge-Density Wave in Cuprate Superconductors: Impact of Aslamazov-Larkin Vertex Corrections*, Phys. Rev. Lett. **114**, 257001 (2015).
- [7] R. Tazai, Y. Yamakawa, and H. Kontani, *Emergence of charge loop current in the geometrically frustrated Hubbard model: A functional renormalization group study*, Phys. Rev. B **103**, L161112 (2021).
- [8] H. Kontani, *Anomalous transport phenomena in Fermi liquids with strong magnetic fluctuations*, Rep. Prog. Phys. **71**, 026501 (2008).
- [9] H. Kontani, R. Tazai, Y. Yamakawa, and S. Onari, *Unconventional density waves and superconductivities in Fe-based superconductors and other strongly correlated electron systems*, Adv. Phys. **70**, 355 (2021).
- [10] T. Moriya and K. Ueda, *Spin fluctuations and high temperature superconductivity*, Adv. Phys. **49**, 555 (2000).
- [11] R. Tazai, S. Matsubara, Y. Yamakawa, S. Onari, and H. Kontani, *A Rigorous Formalism of Unconventional Symmetry Breaking in Fermi Liquid Theory and Its Application to Nematicity in FeSe*, Phys. Rev. B **107**, 035137 (2023).
- [12] T. Hirata, Y. Yamakawa, S. Onari, and H. Kontani, *Unconventional orbital charge density wave mechanism in the transition metal dichalcogenide $1T-TaS_2$* , Phys. Rev. Research **3**, L032053 (2021).
- [13] T. Park, M. Ye, and L. Balents, *Electronic instabilities of kagome metals: Saddle points and Landau theory*, Phys. Rev. B **104**, 035142 (2021).

- [14] R. Nandkishore, L. S. Levitov, and A. V. Chubukov, *Chiral superconductivity from repulsive interactions in doped graphene*, Nat. Phys. **8**, 158 (2012).